UNIVERSITAT ROVIRA i VIRGILI
Facultat de Química

LIGHT DRIVEN HYBRIDE NANOROBOTS FOR WATER REMEDIATION

Master in Synthesis, Catalysis and Molecular Design

Nguyen Xuan Dieu Linh

Supervised by Dr. Bahareh Khezri

Universitat Rovira I Virgili

Acknowledgement

First, I would like to thank my supervisor Dr. Bahareh Khezri for giving me the opportunity to work in this incredible subject and expand my knowledge in chemistry. She provided me a new perspective in research and the freedom to explore new ideas, thus allowing me to make the best decisions for my future career.

Every result described in this thesis was accomplished with the technical and knowledge support from all the Scientific & Technical Resources Service technicians, especially Sònia, Francesc, Mariana, Rita, Eric, and Sergi. I want to express my gratitude to all of them. I thank the other members of Professor J.R. Galán-Mascarós group in ICIQ, Spain for their kindness, support, and help. I am indeed obliged and sincerely thankful to all the friends, juniors, seniors, and coordinators from Erasmus Mundus in the Sustainable Catalysis program for their encouragement and support during my time in Tarragona. All of them have contributed in some way to this project, and they all have my sincere gratitude for being exceptional chemists and people.

I would like to make a special mention to some of the closest people who gave me mental and physical support. I am deeply grateful to Marisa Sanchez and Thi Phuong Anh Vu (Stephanie), who have been by my side since the very beginning of my master's study. They always lifted me and encouraged me when I felt doubtful about myself. Additionally, heartfelt thanks to my sister, Khanh Linh Nguyen, who has supported me and tolerated my stresses and complaints. Their unconditional love, understanding, and encouragement have empowered me to confront and overcome the difficulties of this master's study.

Finally, I would like to thank my family, to whom I dedicate this thesis. Thank you for believing in me more than I believe in myself. Thank you for encouraging me to make crazy life decisions and for loving me just the way I am.

Abstract

Advancements in light-driven microswimmers have marked a significant milestone in the utilization of solar energy for environmental applications, particularly in water remediation. In this work, bismuth vanadate ($BiVO_4$) microswimmers, varying in shape and size, have been successfully fabricated using straightforward, quick, and surfactant-free microwave-assisted and hydrothermal methods. We demonstrated that the morphology of these $BiVO_4$ microswimmers could be fine-tuned by modifying the pH, the concentration, type of the base, and the temperature during synthesis. The photocatalytic capabilities of these microswimmers were evaluated by their effectiveness in degrading emergent pollutants under visible light. Remarkably, their photocatalytic performance was significantly enhanced when $BiVO_4$ was combined to form a heterojunction with $Cs_2AgBiBr_6$ Quantum Dots (QDs), are attributed to QDs role in improving movement speed, facilitating charge regeneration, and reducing the recombination rates of electron-hole pairs. This research lays the groundwork for developing cost-efficient and highly effective $BiVO_4$-based microswimmers, offering a promising solution for large-scale water purification using solar energy.

Table of Contents

Table of Figures

Abbreviations

URV	Universitat Rovira i Virgili
ICIQ	Institut Català d'Investigació Química
QDs	Quantum Dots
BVO	$BiVO_4$
FT-IR	Fourier Transform Infrared
FE-SEM	Field-emission Scanning Electron Microscope
HR-TEM	High-resolution Transmission Electron Microscopy
EDX	Energy-dispersive X-ray Spectrometer
UV-Vis DRS	Ultraviolet-Visible Diffuse Reflectance Spectroscopy
XRD	X-ray Diffraction
ROS	Reactive Oxygen Species
OA	Oleic Acid
OLAM	Oleylamine
ODE	1-octadecene
NCs	Nanocrystals

Chapter 1: Introduction

1. INTRODUCTION TO MICROSWIMMER

Less than 1% of the Earth's freshwater reserves is consumable for human in daily life since clean water scarcity results from the industrialization, population expansion, and climate change. The current water remediation technique such as water chlorination and desalination, advanced oxidation processes and nanotechnologies, are often suffered from the elimination of most pollutants or discharge various harmful by- products into the environment. When introduced into the aquatic ecosystem, contaminants can lead to irreversible accumulative effects, including recurrence, carcinogenicity, mutagenicity, and other human health-related harmful consequences as these contaminants move through the food chain (especially in developing regions)[1]. The high demand for water consumption in industrial sectors force them to adjust to the shortage of clean water resources and to necessitate innovative approaches for the reuse of grey water (e.g., from washing machines and dishwashers) and natural water to guarantee a stable supply of drinking water. Therefore, the enhancement of water remediation treatments by intelligent devices has been discovered and developed.

The application of self-propelled programmable synthetic robots at the micro- and nanoscale holds great potential as an alternative approach to improve water remediation by overcoming diffusion-limited reactions and promoting interactions with target pollutants, including nano- and micro-plastics, persistent organic pollutants, heavy metals, oils, and pathogenic micro-organisms[2]. The requirement of more precise control and intelligent operations agents in complex environments has raised the interest in the study of micro- and nanoswimmers. In general, robots are devices designed to carry out specific tasks either independently or under human control. With the use of teleoperation techniques, robotic devices can enhance sensation and manipulation capabilities, allowing them to reach hazardous or difficult-to-access environments. Small-scale robots, often labeled as 'micro- and nanomotors' when their size is less than 100 μm, are materials structured at the micro- and nano levels that have the ability to collect the energy from their surroundings and transform it into locomotion[3]. The synergy between their mobility and their distinctive physicochemical properties that are determined from the size, shape, and structure at the micro- and nanoscale brings them many advantages over the passive devices.

2. CLASSIFICATION OF MICROROBOTS

In terms of size and shape, micro- and nanorobots are classified into four types: nanowire, nanohelix, tubular, and janus. Tubular micromotors display a multilayer design, which is about 5 to 15 μm in length with an adjustable tube opening diameter of 1 to 5 μm. The outer layer of these microrobots can be made of a polymer or a two-dimensional carbon nanomaterial, while the inner layer consists of a catalyst such as platinum, manganese dioxide, silver, or zinc[4]. Janus are another class of microswimmers, which display an asymmetric morphology with a spherical shape. They are characterized by surfaces that exhibit two or more different physical properties, allowing them to simultaneously perform two different types of chemical reactions[5] [6]. Nanowire microrobots are elongated, wire-like structures typically made from materials such as metals, semiconductors, oxides, and polymers[7]. They often measure in the range of nanometers in diameter and micrometers in length. Nanohelix microrobots are distinguished by their spiral or helical structure that resembles a corkscrew[8]. They are generally constructed from materials like metals (such as nickel or iron), polymers, or composite materials. The nanowire and nanohelix shapes are mostly fabricated for biomedical applications due to their small size and distinctive characteristics.

In term of propulsion mechanism, these swimmers are mainly divided into two types: chemically powered or externally field powered. For chemically driven microrobots, chemicals attached on the material's surface can react with the liquid environment to generate numerous bubbles for propulsion[9]. Hydrogen peroxide (H_2O_2) is the most common chemical for chemically powered swimmers; however, the inherent toxicity associated with chemical fuels has limited their applications in biomedical fields. In contrast, external field propulsion uses optical, magnetic, acoustic, or electric fields to achieve more flexible and sustained control over the robot. Since external field drives do not rely on chemical fuels in the environment, they are more suitable for biological applications. Their size also imposes some limitations due to the limited amount of fuel they can carry, leading to the use of diverse propulsion mechanisms to move these micro-swimmers.

Among the commonly used external energies, light, as an electromagnetic wave, serves as an effective stimulus for propelling microswimmers. It enables remote control, superposition, and spatial and temporal manipulation[10]. Because of these benefits, light-driven microswimmers are becoming increasingly popular in the development of these tiny swimmers. The facile accessibility, simple design and cost-effectiveness of light-driven micro- and nanorobots systems demonstrate it highly promising for the wide-range environmental treatment applications. In addition, the wireless transmission and remote controllability of light-driven micro- and nano swimmers show their faculty of indirect manipulation, which could be further used in complex or toxic media. Due to these

advantages, light-driven microrobots are leading candidates for environmental remediation. In the next part, we will focus on the mechanism and catalytic activity of light-driven microrobots.

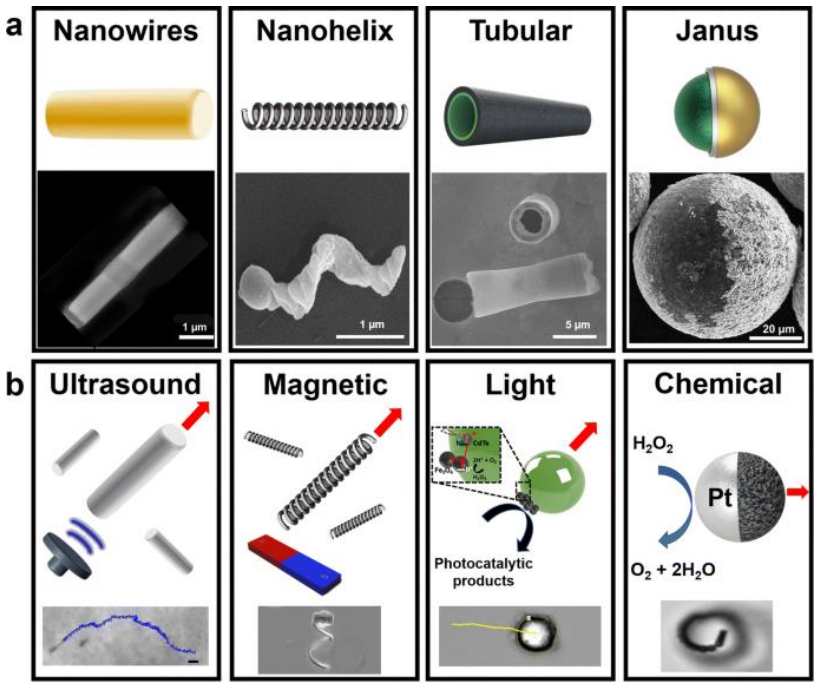

Figure 1: Classification of microrobots according to: (a) Morphology and size, (b) Propulsion mechanism[4]

3. LIGHT-DRIVEN MICROROBOTS

3.1. Movement mechanism of light-driven microrobots

Light-propelled microswimmers can be driven by four mechanisms, including self-diffusiophoresis, electrophoresis, thermophoresis and bubble-based propulsion[11] (Fig. 2). Based on their driving mechanisms, light-powered microrobots can be categorized into five main types: those driven by photochemical reactions, photothermal effects, photomechanical effects, optical tweezers, and other driving mechanisms[12]. Light-driven microswimmers are prepared from light-sensitive materials, including photocatalytic, photolytic, photoisomerized, photothermal, and photochromic materials[13].

The earliest recognized mechanism of propulsion for nano- and micromotors was bubble propulsion[14]. The predominant approach to generate bubbles involves the catalytic decomposition of H_2O_2 into O_2 that is facilitated by a Pt catalytic layer. In tubular micromotors, the movement is provoked by the growth and expulsion of O_2 bubbles from one side. For spherical micromotors that have catalytic and functional layers distributed across half of the sphere's surface, H_2O_2 decomposition occurs on the hemispherical section covered by the catalytic layer[15]. The periodic generation of the bubbles and the interaction between the bubble and micromotors are the driving

forces of their motion. The light-driven bubble propulsion of nano- and micromotors can be achieved by taking advantage of photocatalytic reactions; for example, the movement of TiO_2 tubular micromotors by photocatalytic decomposition of H_2O_2 on its surface under UV irradiation[16].

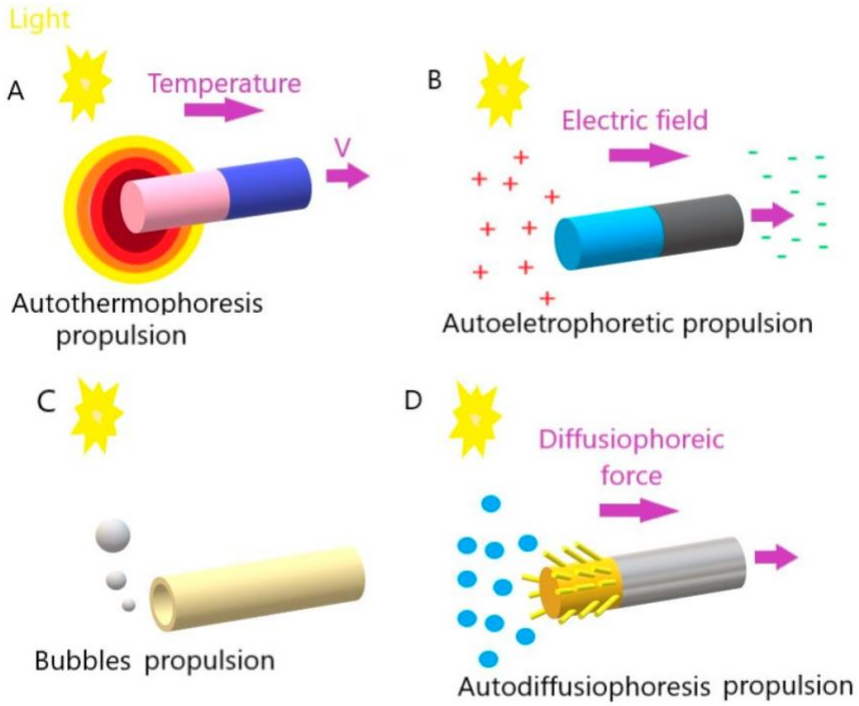

Figure 2: Different methods of light-triggered propulsion in synthetic microswimmers[14]

The light-driven self-electrophoretic propulsion is the most common mechanism, which can be classified into chemical gradient and temperature gradient[17]. Self-electrophoretic propulsion relies on light to induce an electric field, then particles respond to an electric field by playing the movement. It is important to note that the response to light illumination may differ depending on the materials involved, such as metals and semiconductors, which will affect the type of reaction occurring on the materials surface. Thermophoresis, commonly known as the Soret effect, is caused by the temperature gradient, which means the nanoparticles will move from the hot and high energy region to the cold and lower energy region. In global illumination conditions, the temperature gradient near the particle can induce thermal diffusion within the fluid, resulting in the propulsion of the particle[18]. Diffusiophoresis typically describes the movement of a particle caused by pressure and electric fields generated by differential diffusion of specific anions and cations [18]. In this case, nano- and micromotors operate based on a concentration gradient of solute across their surface, which causes a directional flow of water from regions with lower to higher solute concentrations, thus driving the movement.

3.2. Manipulation methods

The precise modulation of micro- and nanomotor dynamics is crucial for their multipurpose applications, especially in environmental remediation and cargo transportation. Overcoming challenges posed by strong Brownian motion at the micro- and nanoscale, light-driven microrobots offer a strategic solution and use light as an external physical field for their activation. The manipulation of parameters such as the direction, intensity, wavelength, and polarization of visible light are some important factors to control the motion behavior of micro- and nanorobots. Some of the most common control strategies for light-driven microrobots are speed control, directional control, and cluster control methods[19].

3.2.1. Speed control

Adjusting the light intensity is a straightforward method to control the speed of microrobots. The stronger the intensity of light, the faster the movement of these swimmers. The on and off motional control is simply attained by switching visible light, which was demonstrated by a study on the motion control of light-driven catalytic gold decorated soft-oxometalate-based nanomotors for organic pollutant remediation[20]. Another approach is to combine a light field with an external physical field to control the speed of micro- and nanorobots.

3.2.2. Directional control

The magnetic field is usually used as an external energy source to control the direction of micro- and nanorobots, and it normally targets the biomedical application such as functional cellular analysis, disease diagnosis and treatment, targeted drug delivery, and micro-surgery monitoring[21]. However, magnetic-controlled robots require advanced equipment and extra space for the magnetic-generating device. While the majority of microrobots can be directed by an external magnetic field, light-driven counterparts exhibit phototaxis or negative phototaxis behavior, which allows directional control by altering the position of light source without the use of external magnetic power[22]. Fig. 3a describes in more detail the motional control of robots by changing the direction of incoming light. The phototaxis and negative phototaxis behaviors of micro- and nanorobots arise from their asymmetric structure or asymmetric exposure to light, thus inducing asymmetrical chemical reactions. Furthermore, the shape of the swimmers can affect the direction of their movement, which was demonstrated by the study of Wang et. al[23].

3.2.3. Cluster behaviour control

The grouping behaviors of multiple micro- and nanorobots overcome the limitation of the load capacity and moving distance of individual micro- and nanorobots. Under visible-light exposure,

visible-driven microrobots show different cluster forms (Fig. 3b). Diverse approaches have been employed to manipulate the collective behavior of light-driven swimmers, especially focus on the achievement of more refining control strategies. However, the current methodologies are relatively simple because they just allow the movement or aggregation in two dimensions. The application of light source alone is insufficient to meet further requirements, thus provoking the demand for the integration of multiple physical fields coupling for the more precise control of visible-driven micro- and nanoswimmers. This technique will allow three-dimensional motion and aggregation, and it is expected that the employment of artificial intelligence could also lead to better collective behavior control.

a b

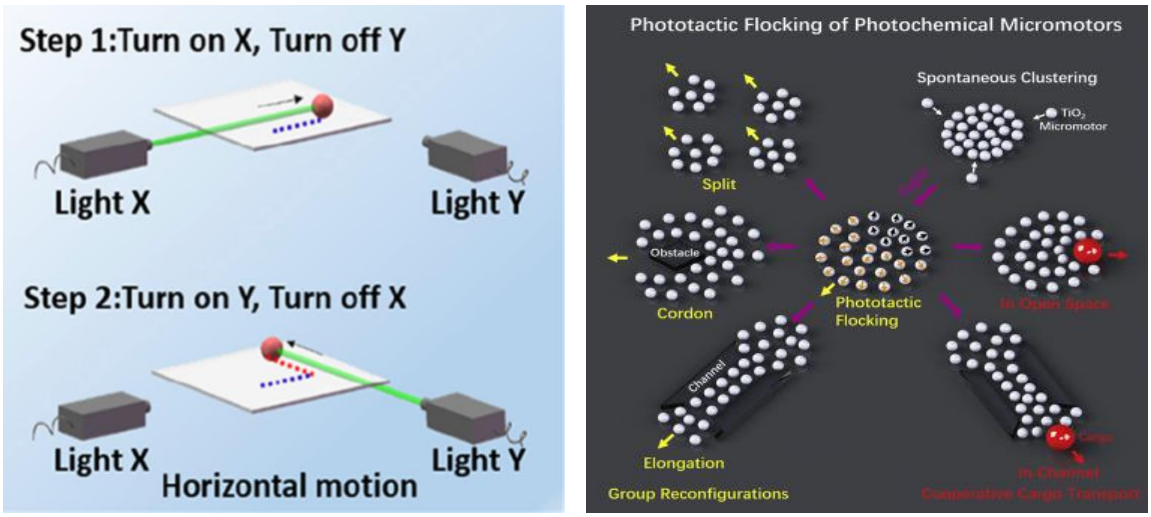

Figure 3: The control of light-driven microrobots by: (a) Adjusting the direction of light incident[24], (b) Controlling collective motions and tactic behaviors[25]

3.3. Photocatalytic microrobots - $BiVO_4$

In recent years, there has been an increasingly investigation and broad utilization of photocatalytic technologies in various fields including water splitting, organic pollutant degradation, carbon dioxide reduction and so on. Up to now, the focus of research has predominantly focused on utilizing titanium dioxide (TiO_2) photocatalysts for energy and environmental applications due to their remarkable photocatalytic efficiency, non-toxic nature, and strong stability under light exposure[24]. However, TiO_2 only exhibits sensitivity to UV light, which means it utilizes just 4% of the solar energy spectrum, thus restricting its potential applications. Therefore, the development of more innovative strategies has been demanded, aiming at optimizing the utilization of solar energy. In recent decades, considerable effort has been directed towards the development of visible light-driven photocatalysts, at which over 150 types of semiconductor materials were discovered and studied for water splitting,

artificial photosynthesis, and the degradation of organic pollutants[25]. They include metal sulfides, metal oxides, oxynitrides, chalcogenides, halides, and oxyhalides[26]. Among them, metal oxides stand out as the semiconductor type that has been largely studied for photocatalytic applications since they have high stability, facile fabrication processes and low cost. However, most binary metal oxides exhibit high band gap energies with high positive valence bands, thus limiting their capacity to absorb light effectively. Ternary metal oxides incorporating elements like Bi, Ag, Pb, or Sn, such as $BiVO_4$, Bi_2WO_6, $AgNbO_3$, $PbCrO_4$, and $SnNb_2O_6$ feature narrower band gaps, thus being promising candidates for visible light-driven photocatalytic studies[27].

In a classical photocatalytic reaction, when photocatalytic materials are exposed to light, they generate electrons and holes in the conduction band and valence band, respectively. These electrons and holes will play a redox reaction with water or environmental fuel sources to form ions, molecular species, or gases[28]. A similar mechanism occurs on microrobots surface; however, those products formed create a gradient of species around the surface and thus driving their motion. These photocatalytic materials can be used as microrobots if asymmetric propulsion can be created to form a gradient to propel the microrobots, which means the materials must have asymmetric designs. However, the fabricating asymmetric design is challenging due to the complicated fabrication methods and low efficiency of most photocatalytic materials. Even though these materials may play a good role in producing gas products such as hydrogen or oxygen, these reactions often proceed slowly and inefficiently. For the sustained propulsion of light-driven micromotors, the driving force must be strong enough to propel the swimmers for a long time[10].

Bismuth-based metal oxide ($BiVO_4$, Bi_2MoO_6, Bi_2WO_6, $BiFe_2O_3$, $BiFe_4O_9$, and BiOX (X = halogens) have been regarded as emerging photocatalysts because of their narrower bandgap and have ability to enhanced charge transfer. Bismuth vanadate ($BiVO_4$) has gained considerable attention because of its remarkable characteristics, including a narrow band gap (E = 2.4 eV)[29], excellent dispersibility, non-toxicity, favorable valence band position, ferro elasticity, photochromic effect, ionic conductivity, long-term photostability, resistance to corrosion, and good photocatalytic activity in degrading pollutants, oxygen production, and carbon dioxide reduction under visible-light irradiation[30 31]. In general, $BiVO_4$ is known to exist in three crystalline phases, namely monoclinic scheelite (m-s), tetragonal zircon (t-z), and tetragonal scheelite (t-s) (Fig. 4). Typically, low-temperature synthesis methods, such as precipitation at room temperature, yield t-z $BiVO_4$, and high-temperature synthesis techniques, such as solid-state and melting reactions, lead to the formation of m-s $BiVO_4$[32]. Among these crystalline phases, m-s $BiVO_4$ has been favored compared to the other two crystalline phases because of its greater photocatalytic performance under visible-light irradiation.

The lone pair distortion of the Bi 6s orbital within the m-s $BiVO_4$ semiconductor results in a unique overlap between the O 2p and Bi 6s orbitals in the valence band (VB), which facilitates the mobility of photogenerated charge carriers, thus giving an improvement in photocatalytic activity[33]. Unfortunately, as a single-phase photocatalyst, $BiVO_4$ exposes a rapid recombination of photoexcited electrons and holes in the conduction and valence bands due to its low surface area and poor charge transfer, thereby restricting its photocatalytic performance. To overcome this challenge, significant efforts have been directed towards enhancing the separation of photogenerated charge carriers. Various strategies have been pursued, including morphology control, metal[34] and non-metal[35] element doping, creating semiconductor heterojunctions[36 37 29 38], etc.

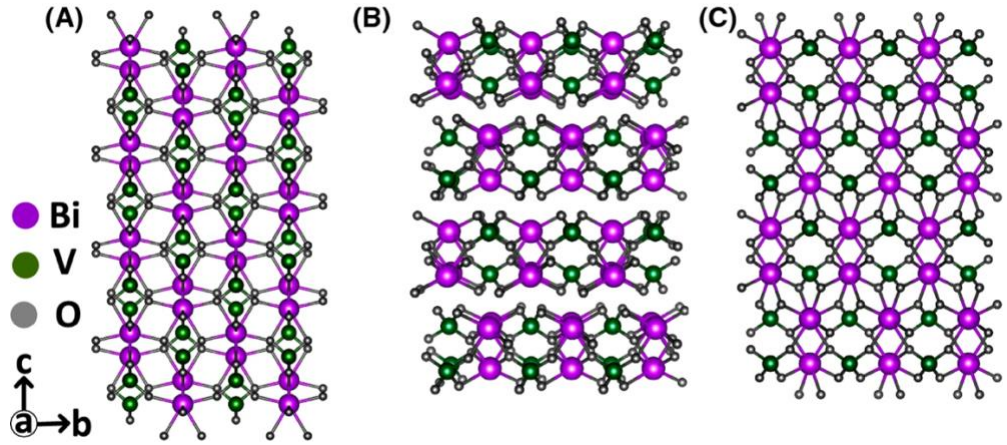

Figure 4: Crystal structure of $BiVO_4$: (a) tetragonal zircon, (b) monoclinic scheelite, and (c) tetragonal scheelite[41]

$BiVO_4$ particles are interested in microswimmer systems based on their efficient separation of electrons and holes between the {010} and {110} crystal facets under visible light without the need of a cocatalyst[39]. In the field of light-driven micro- and nanoswimmers, $BiVO_4$-based systems are recognized as ideal candidates as the synthesis methods are inexpensive and uncomplicated. Depend on their morphology, $BiVO_4$-based microswimmers exhibit interesting swimming behaviors, which are driven by photogenerated fluid flows, interactions with the substrate, and/or the influence of external entities[40]. However, without the present of fuel, the driving force of $BiVO_4$ is not strong enough to move sustainably, and their catalytic activity toward organic pollutant is still low. The grafting of $BiVO_4$ with another material is demanded to enhance its motion and photocatalytic activity.

Among many semiconductor materials used for photocatalytic applications, halide perovskites have recently gained attention as promising photocatalysts due to their outstanding properties, such as a tunable band structure, high absorption coefficient, and excellent charge separation efficiency[41]. Toxicity and instability are the main concerns of inorganic perovskite as the material is composed of

toxic Pb^{2+} cations; therefore, lead-free halide perovskites become promising alternative candidates for photocatalytic applications. Among the various lead-free double perovskites, $Cs_2AgBiBr_6$ has proved its superior stability against moisture, air, heat, and light[42]. Cubic $Cs_2AgBiBr_6$ is characterized by ordered double $[AgBr_6]^{5-}$ and $[BiBr_6]^{5-}$ octahedra with alternating Ag^+ and Bi^{3+} ions at the B and B' sites, and Cs^+ ion filled in the gaps, thus making it has high optical absorption coefficient and suitable electronic band structure (Fig. 5). $Cs_2AgBiBr_6$ possesses an indirect bandgap measured between 1.95 eV [43] and 2.19 eV [44], which can be used to as composite to lower bandgap of other semiconductors. The photoelectric properties of $Cs_2AgBiBr_6$ were demonstrated to be well-tailored by its lower dimensional confinement effects, especially for quantum dots (QDs) design[45].

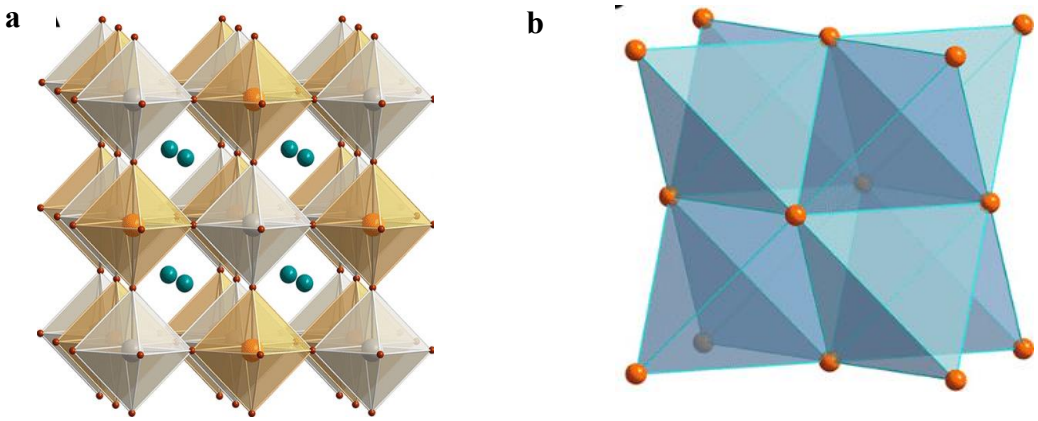

Figure 5: (a) Crystal structure of $Cs_2AgBiBr_6$ Orange, grey, turquoise, and brown spheres represent Bi, Ag, Cs, and Br atoms. (b) The edge-sharing tetrahedra of a Bi^{3+} face-centred-cubic sublattice[49]

4. MICROROBOTS FOR WATER TREATMENT

In compare with the traditional methods like filtration, adsorption, and catalytic degradation, light-driven micro- and nanorobots pose unique advantages as they can enhance the adsorption, the decomposition and sensing processes. These tiny robots are designed to speed up and improve water remediation through the synergistic interplay of their active motion and material characteristics to enhance the adsorption of soluble organic pollutants and heavy metals at the solid–liquid interface. Microswimmers can be engineered to display a surface charge opposite to that of the target contaminants through functionalization with specific molecules or polymers, or by altering solution parameters[46].

Macrolides have been used in medical treatments for almost 80 years since the discovery of erythromycin in 1949. Second-generation macrolides, including synthetic derivatives like clarithromycin, roxithromycin, and azithromycin have been developed and applied in treating human infectious diseases such as community-acquired bacterial pneumonia, gonorrhea, etc[47]. However, the

extensive use of macrolides in both industry and household has led to the development of resistance, particularly in gram-positive cocci (such as staphylococci, streptococci, and pneumococci) and gram-negative bacteria (including enterobacteria and Haemophilus influenzae)[48]. Hence, the elimination of the macrolides in aqueous environment is necessary.

In this report, the double-perovskite $Cs_2AgBiBr_6$ QDs were incorporated into $BiVO_4$ microrobots to obtain a novel $BiVO_4{-}Cs_2AgBiBr_6$ composite for sustainable and effective water remediation.

Chapter 2: Aims and Objectives

This thesis focuses on synthesizing $BiVO_4$ microrobots and enhancing their movement and photocatalytic efficiency by forming a heterojunction with $Cs_2AgBiBr_6$ QDs. The motion behaviour and catalytic activity of these microrobots under light illumination. Since then, our work will be divided in 2 parts:

- Optimize the synthesized condition for $BiVO_4$ microrobots and grafting them with $Cs_2AgBiBr_6$ QDs
- The study of motion and photocatalytic activity of our prepared microrobots toward antibiotic degradation

Firstly, the screening and optimization of the synthesized condition for $BiVO_4$ microrobots had been carried out. A hydrothermal approach was investigated to achieve this goal, and then the grafting with $Cs_2AgBiBr_6$ QDs by simple mixing were performed. Several characterization methods were applied to check the morphology of our compounds, including SEM, TEM, XRD, UV-Vis DRS, FT-IR, Raman, and Zeta-potential measurement. The formation mechanism of $BiVO_4$ at different pH was proposed, and the impact of $Cs_2AgBiBr_6$ QDs on the based $BiVO_4$ compound was studied.

Secondly, the catalytic activity of the prepared microrobots under light illumination was checked. The catalytic performance of microrobots against certain emerging pollutants was evaluated, and a degradation mechanism was suggested.

Chapter 3: Results and Discussions

1. CHARACTERIZATION OF MORPHOLOGY AND STRUCTURE

1.1. Morphology measurement of $BiVO_4$

The shape and size of microrobots are important for studying their movement and catalytic activity. SEM measurements were conducted to study the influence of pH on particle size and shape of $BiVO_4$. The FE-SEM images of the synthesized $BiVO_4$ in different pH using NaOH and NH_3 solution as solvents are shown in Fig. 6 and Fig. 7, respectively.

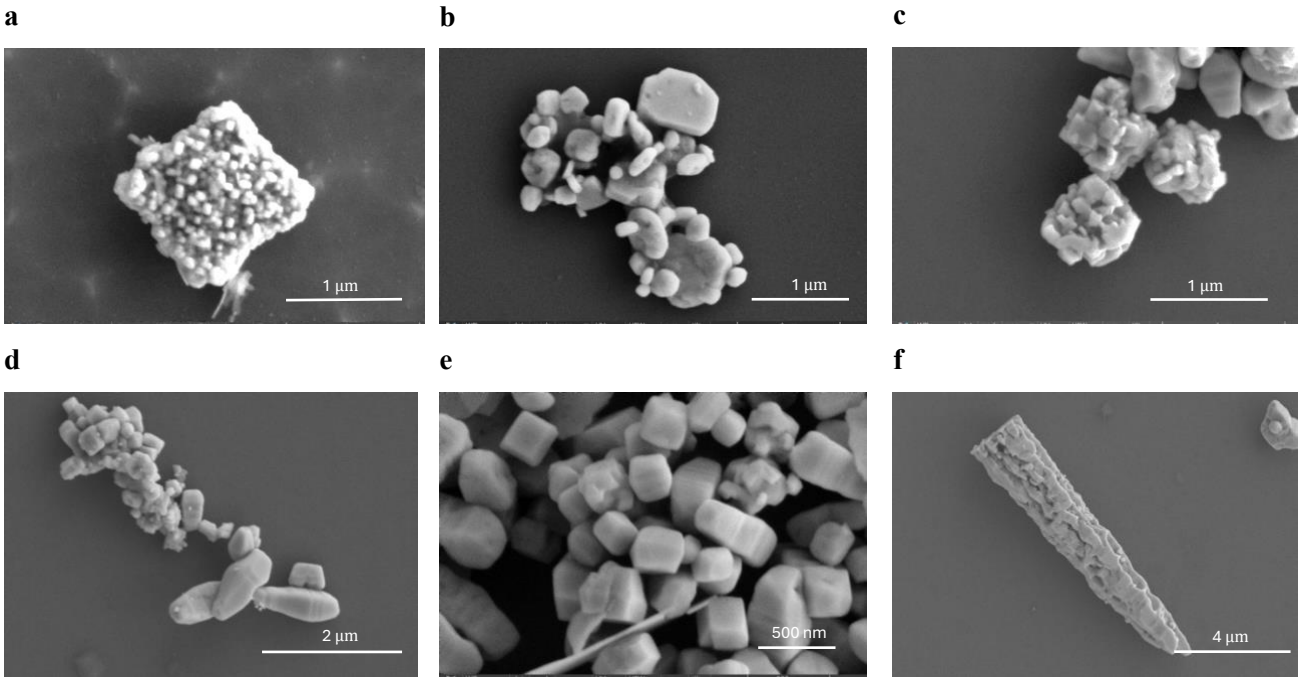

Figure 6: The FE-SEM images of $BiVO_4$, synthesized at pH 1 (a), 2 (b), 4 (c), 6 (d), 7 (e), 8 (f), using NaOH as solvent

The SEM images showed that the $BiVO_4$ microrobots appeared in irregular shape with various degree of agglomeration of particles. In a lower pH value (acidic medium), small-sized nanocomposites are formed. As the pH increased, the particles tended to accumulate and form a rod shape. The development of various morphologies and the shift from particles to rods is entirely dependent on the experimental conditions, reaction mechanisms, and material formation processes[49]. These shape variations arise from differences in crystal arrangement, preferential growth along specific orientations, atomic radii, and chemical reactions occurring during the hydrothermal process[50]. In conclusion, our SEM results indicate that the conversion of particles into rod shapes progresses as the pH increases during the synthesis of $BiVO_4$ microrobots using NaOH as a diluted base.

In contrast, there is no specific revolution route for the variation in the shape of $BiVO_4$ using ammonia solution as a diluted base. The fishbone shape of $BiVO_4$ was obtained at pH values of 2 and 8; however, the synthesis at pH 2 resulted in a 3D morphology, while a 2D morphology was observed at pH 8. The fishbone morphology of $BiVO_4$ can be attributed to Brownian motion or the growth of particles into rod-like structures[51]. However, as the pH increased, the agglomeration phenomenon of the $BiVO_4$ seemed to become more obvious, thus leading to an increase in particle size.

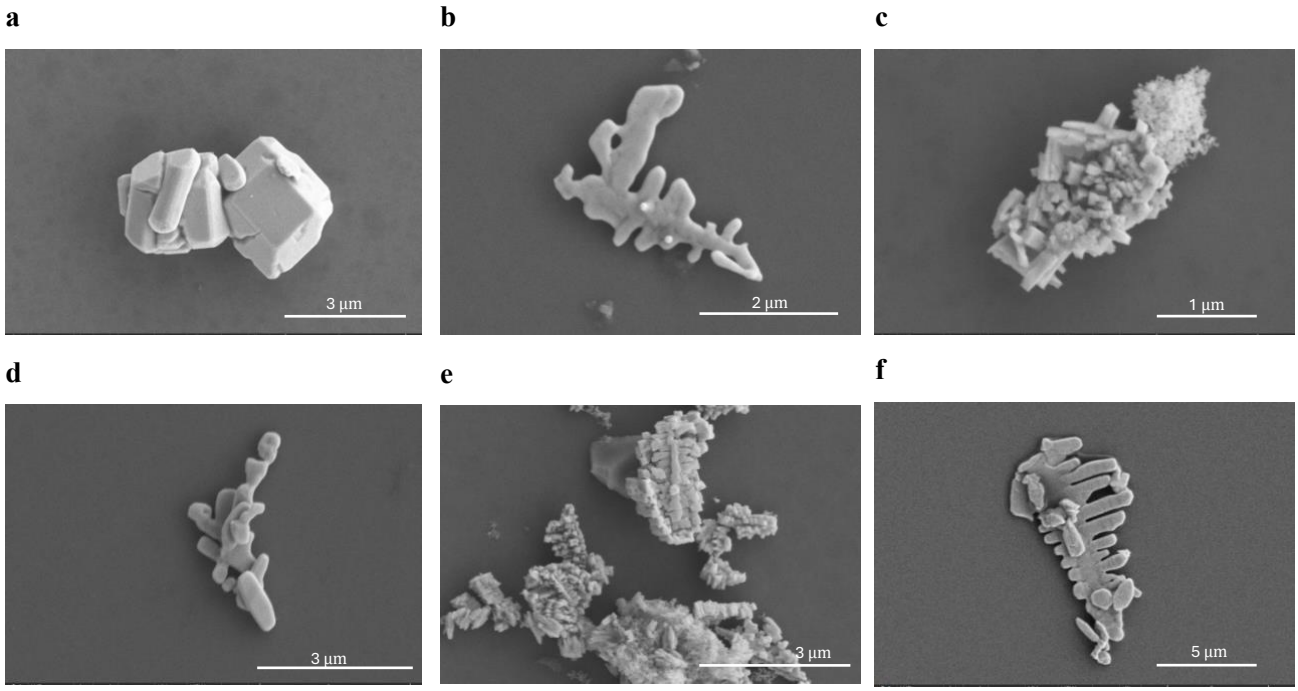

Figure 7*:* The FE-SEM images of $BiVO_4$, synthesized at pH 1 (a), 2 (b), 4 (c), 6 (d), 7 (e), 8 (f), using NH_3 as the solvent

The different morphologies arise from the balance between nucleation and growth rates, which are controlled by the pH-dependent speciation and solubility of the precursor ions. This phenomenon is well-documented in materials science, where the pH influences the hydrolysis and condensation reactions during the synthesis of metal oxides[52]. Since then, the formation mechanism can be proposed as follows:

In an acidic environment, Bi^{3+} ions remain relatively stable while the vanadate ions ($VO_4{}^{3-}$) tend to form polyvanadate species like $HVO_4{}^{2-}$, $H_2VO_4{}^-$ and H_3VO_4. After mixing, these species interact with Bi^{3+} ions and lead to the formation of small, uniform nanoparticles. The high concentration of H^+ ions facilitate the rapid nucleation of small particles. As can be seen from the SEM result, at pH 1 and 2, small-sized $BiVO_4$ particles are formed due to the high nucleation rate and limited growth phase.

As the pH increases, Bi^{3+} ions begin to hydrolyze, thus forming various hydroxide species such as $Bi(OH)^{2+}$ and BiO^{+}. These species act as nucleation sites, promoting the growth of larger particles and eventually forming rod-like structures. The stability of $VO_4{}^{3-}$ in these conditions supports the straightforward formation of $BiVO_4$. It can be seen from the SEM images of samples synthesized at pH 6 to 8, $BiVO_4$ particles transition to rod-like shapes due to slower nucleation but prolonged growth phases, facilitated by the stable presence of $VO_4{}^{3-}$ ions.

The movement of some selected $BiVO_4$ samples were checked by Confocal Microscopy to confirm the mobility of our microrobots. From SEM and microscopy results, we chose the sample $BiVO_4$ synthesized at pH 2 and 8 for further studies. We denote them as BVO-2 and BVO-8. For their composites with $Cs_2AgBiBr_6$, we denote them as BVO-QDs-2 and BVO-QDs-8.

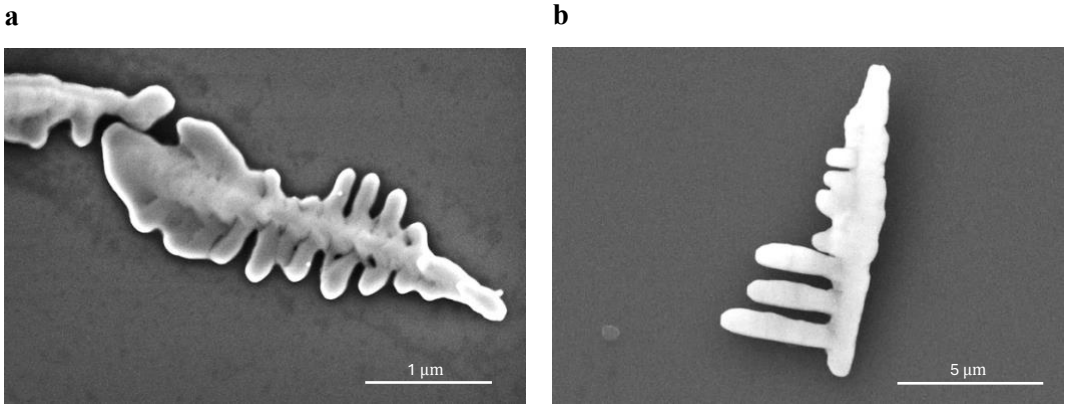

Figure 8: The FE-SEM images of BVO-QDs-2 and BVO-QDs-8 sample

The FE-SEM images of samples BVO-QDs-2 and BVO-QDs-8 are showed in Fig. 8. The morphology and structure of BVO-QDs composites cannot be observed by FE-SEM measurement. Hence, the HR-TEM analysis was carried out to confirm the structure of our composite.

To understand and confirm the successful grafting of BVO-QDs-2 composites, a detailed HR-TEM characterization was carried out. Fig. 9a presents the HR-TEM measurement of our composite using high-intensity electron beam. The small particles attached to the $BiVO_4$ fishbone structure represented the $Cs_2AgBiBr_6$ nanoparticles with a diameter of around 4 nm (Fig 9d). The dark and bright field images were taken to observe the existence of heavy metals on $BiVO_4$ surface (Fig. 9b & 9c). In bright field mode, the regions with heavier atoms are darker as the heavier atoms scatter electrons more intensely than lighter atoms, while in dark field mode, these regions are brighter. The $Cs_2AgBiBr_6$ QDs strongly diffracted as they appeared darker in the bright-field mode and brighter in the dark-field mode; hence, the compound might be more crystalline.

This result indicated that BVO-QDs-2 microrobot had been successfully synthesized in company with XRD analysis.

The elemental mapping (EDX) was performed to confirm the existence of $Cs_2AgBiBr_6$ QDs on the $BiVO_4$ surface by providing information on the composition of various elements present in the fishbone structure. Figures 10 b-f show the elemental maps of Bi, V, O, Ag, and Br in dark blue, yellow, red, purple, and green, respectively. Fig. 10a presents the overlaid images of all elements, indicating that particle formation on the surface is only contributed by Bi, Br, and Ag since the distributions of V and O are not involved in the particle parts. The EDX results demonstrated the successful attachment of $Cs_2AgBiBr_6$ QDs on the $BiVO_4$ surface of the composite sample that was prepared at pH 2.

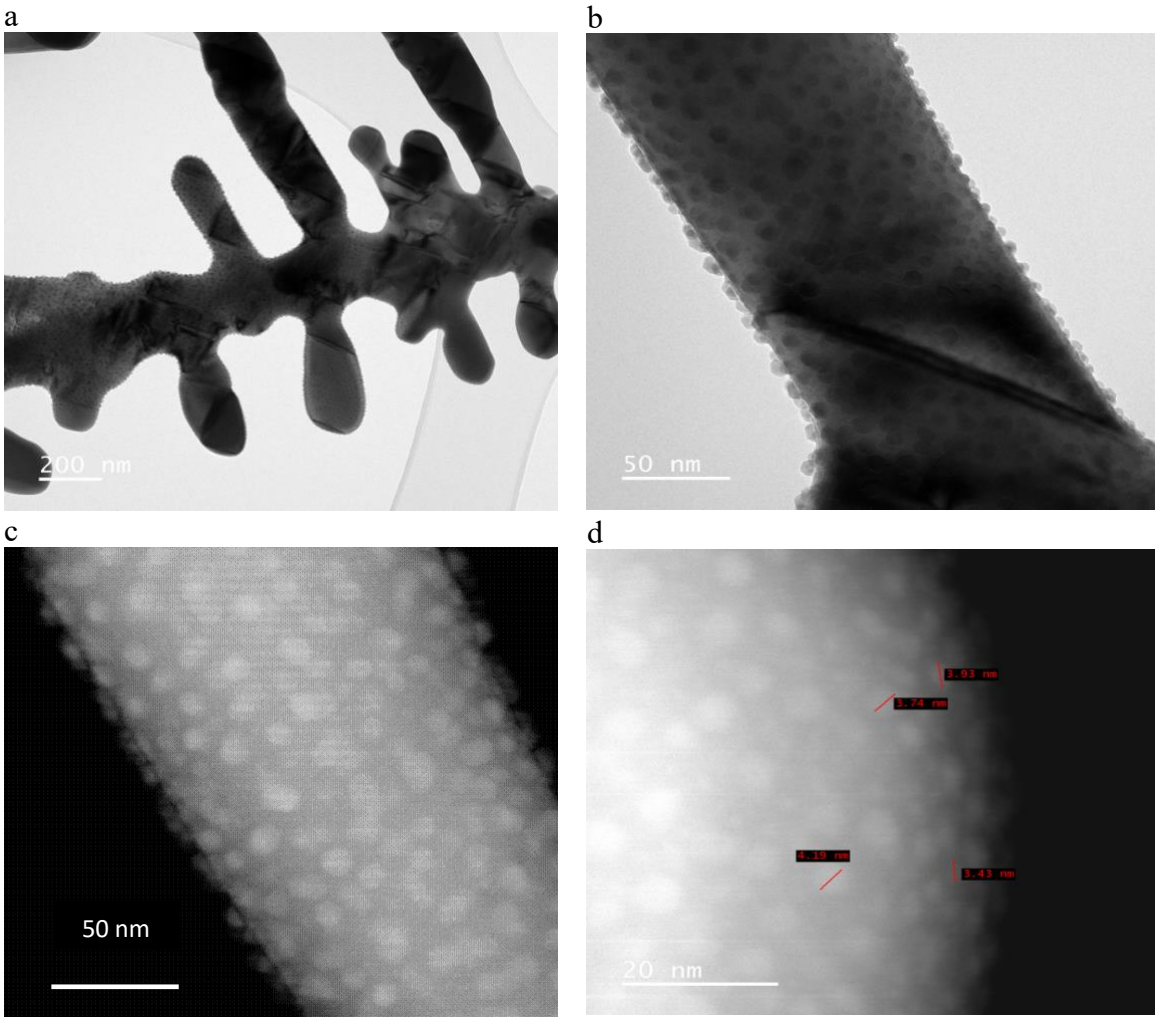

Figure 9: HR-TEM images of BVO-QDs-2 microswimmers: (a) Bright-field TEM image in 200 nm scale bar; (b) Bright field TEM image in 50 nm scale bar; (c) Dark field TEM image in 50 nm scale bar; (d) Dark field TEM image in 20 nm scale bar with particle size measure

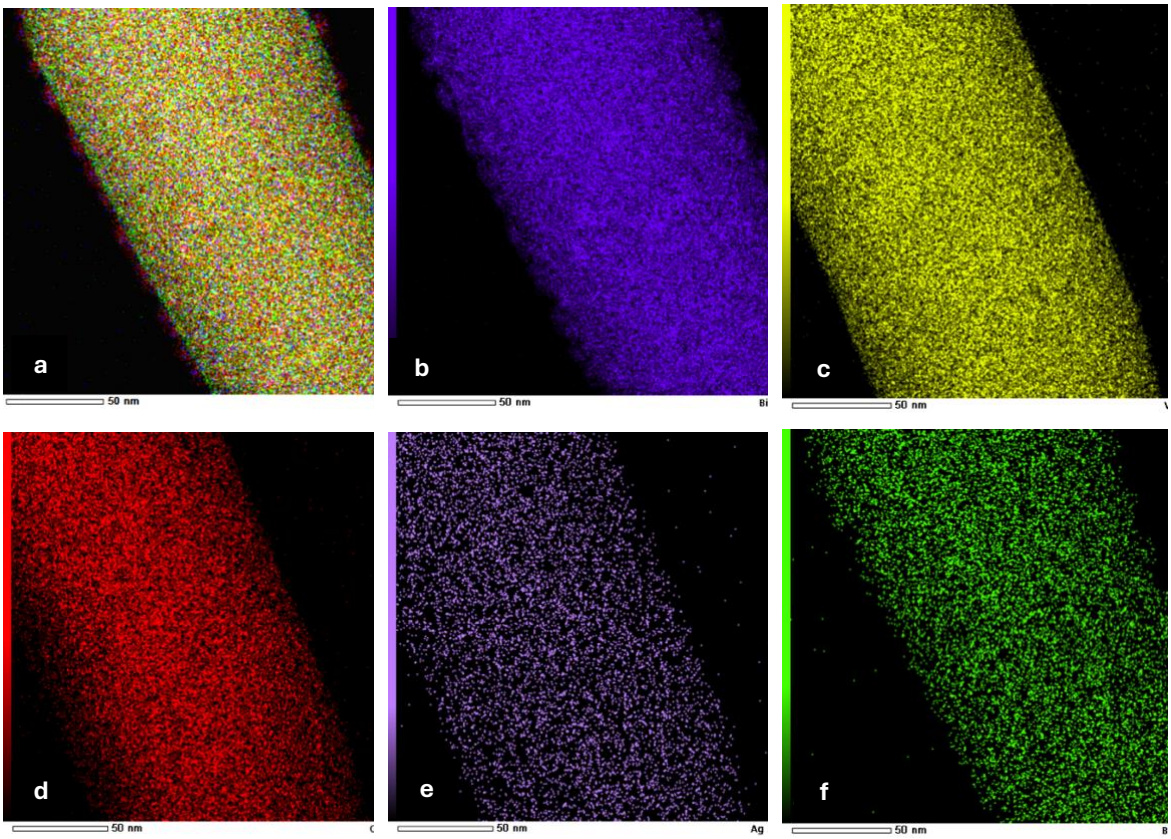

Figure 10: EDX color-coded elemental map of BVO-QDs-2 microswimmers: (a) Combined elements, (b) Bi, (c) V, (d) O, (e) Ag, and (f) Br. The scale bar is 50 nm for all pictures

In contrast, the TEM and EDX measurements of the composite prepared at pH 8 indicated the unsuccessful attachment of QDs on the $BiVO_4$ surface. The TEM images of this sample, shown in Fig. 11, did not reveal any particle formation on the surface of the fishbone structure in either dark or bright field images. Furthermore, the EDX results only confirmed the presence of Bi, V, and O in the compound (Fig. 12). The higher positive charge might lead to repulsion between similarly charged QDs, reducing the likelihood of strong electrostatic attraction.

The $[AgBr_6]^{5-}$ and $[BiBr_6]^{5-}$ octahedra indicate the presence of negatively charged entities within the QDs structure. The presence of Cs^+ ions suggest a balance of charges within the overall structure. Given this information, the QDs are likely to exhibit a net neutral charge overall due to the balancing of positive and negative charges within their structure. However, specific surface charges may vary based on the exact synthesis conditions and the surrounding environment. The $Cs_2AgBiBr_6$ QDs are designed to have a stable structure with alternating positive and negative charges that balance out overall, resulting in a net neutral charge. This balance ensures the stability of QDs sand and enhances

its photocatalytic properties. The interaction with the $BiVO_4$ microrobots are influenced more by surface chemistry and specific binding sites rather than a straightforward positive or negative charge.

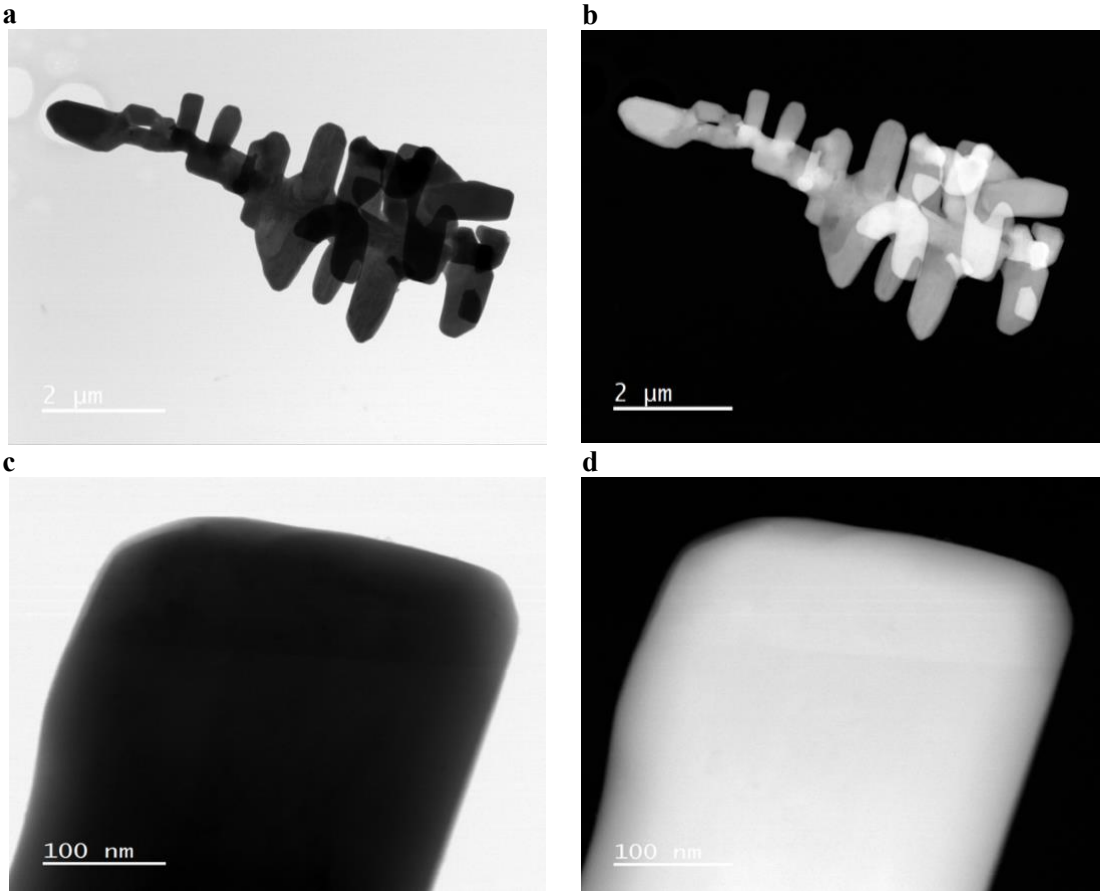

Figure 11: HR-TEM images of BVO/QDs-8 microswimmers: (a) Bright field TEM image in 2 µm scale bar; (b) Bright field TEM image in 2 µm scale bar; (c) Dark field TEM image in 100 nm scale bar; (d) Dark field TEM image in 100 nm scale bar

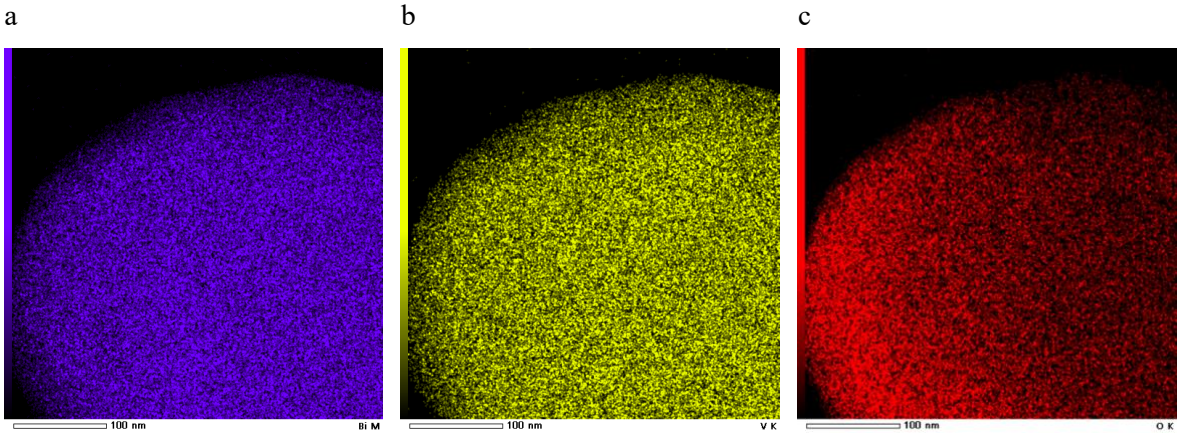

Figure 12: EDX color-coded elemental map of BVO-QDs-8 microswimmers: (a) Bi, (b) V, and (c) O. The scale bar is 100 nm for all picture

1.2. XRD

The XRD patterns shown in Fig. 13a confirmed the monoclinic structure of $BiVO_4$. According to the JCPDS card 75–1867, the XRD peaks of pure monoclinic $BiVO_4$ appear at 11.2°, 18.5°, 25°, 28.2°, 30.6°, 32.8°, 35.3°, 40.2°, 46.6°, 53.7°, and 57.4°. These peaks correspond to diffraction from the (001), (011), (111), (013), (040), (113), (200), (002), (240), (161), and (206) planes of the monoclinic structure. In our diffraction results for the two $BiVO_4$ samples, the most intense peaks at 18.9°, 28.8°, 30.4°, 53.2° were observed, with more than 95% of the monoclinic structure and less than 5% of the tetragonal structure. The correspondence in diffraction patterns demonstrated that the crystal size and structure of $BiVO_4$ were not affected by pH of the synthesis process and the morphology of the sample.

However, there is no difference in diffraction pattern of the other two composite samples. This might be explained by the small amount of QDs grafted on $BiVO_4$ (1%), the extra-small size of $Cs_2AgBiBr_6$ QDs nanoparticles and the short acquisition time (1800 s). The board XRD diffraction peaks indicated the compounds in nano size; however, since there was just about 1% of QDs grafted on BVO, the peaks belong to $Cs_2AgBiBr_6$ might be too insignificant to be observed. Therefore, a longer acquisition time test toward BVO-QDs-2 sample was carried out to check if the board peaks belong to $Cs_2AgBiBr_6$ could be detected.

Fig. 13b illustrates the XRD patterns of the BVO-QDs-2 sample with the longer acquisition time (4150 s). From the matching patterns, the significant peaks at 22.3°, 26.2°, 27.4°and 31.7° belongs to $Cs_2AgBiBr_6$ cubic structure, thus confirming the existence of $Cs_2AgBiBr_6$ QDs in the composites. On the other hand, there is no peak belonging to the QDs compound has been detected in the BVO-QDs-8 sample (Fig. 13c). This can be explained by the unsuccessfully attached of QDs on the BVO-8 surface. The weight distribution of each compound was provided in the Additional Information chapter.

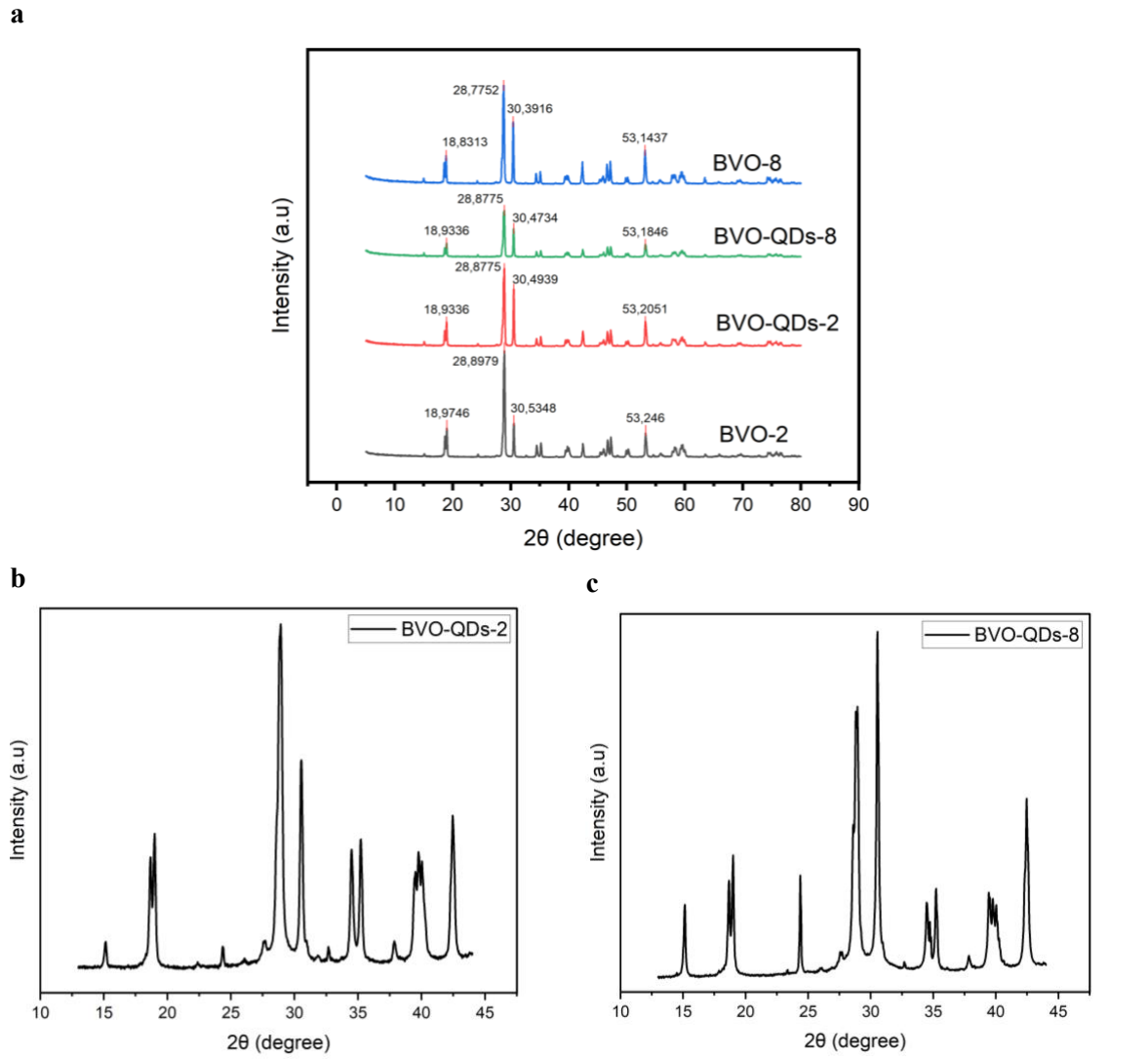

Figure 13: XRD diffraction patterns of (a) BVO-2, BVO-QDs-2, BVO-8, BVO-QDs-8 samples with 1800s of acquisition time; (b) BVO-QDs-2 and (c) BVO-QDs-8 with 4150s of acquisition time

1.3. UV-Vis DRS Analysis

To calculate the electronic states of the semiconductor materials, the DRS was used. The optical characteristics of BVO and BVO-QDs samples were analyzed by UV–Vis spectroscopy, as shown in Fig. 14a. It is seen that the samples exhibited strong absorption abilities in the range of visible light region (400-500 nm). The sharp drop in the recorded absorption line in this region could be explained due to the transition of electrons in the semiconductor material during the absorption. Consequently, the bandgap energy E_g of BVO and BVO-QDs samples could be determined from the Tauc's plot of $h\nu$ vs $(\alpha h\nu)^2$.

In this study, the band energy of our microswimmers was examined using UV-Vis absorption spectroscopy, which revealed a distinct absorption edge at 470 nm for BVO-8 and BVO-QDs-8 samples, and at 450 nm for BVO-2 and BVO-QDs-2 samples. The absorption spectra of $Cs_2AgBiBr_6$ QDs were provided by Palomares's research group, indicating that the QDs compound absorbed light at 420 nm, and its bandgap was calculated to be 2.35 eV (Fig. 14b). The absorption edge marks the initiation of electronic transitions within the material[53]. Utilizing the Tauc plot method, the square of the absorption coefficient $(\alpha h\nu)^2$ was plotted against the energy of incident photons $(h\nu)$. OriginPro software was employed to determine the straight-line fit for the relationship between $(\alpha h\nu)^{1/n}$ and $h\nu$, considering various values of n (1/2, 3/2, and 2). The optimal fit was specifically investigated for the case where 1/n equals 2, which means the compound allowed a direct transition. The resulting Tauc plot showed a linear region in the high-energy range, suggesting that the microswimmers exhibit characteristics of a direct band gap semiconductor[54]. By extending the linear portion of the plot to the x-axis, the experimentally measured band gap energy was found to be 2.4 eV for BVO-8 and BVO-QDs-8 samples, and 2.5 eV for the other samples (Fig. 14c). This obtained results suggested that the adding of $Cs_2AgBiBr_6$ QDs have no significant impact on the bandgap of $BiVO_4$.

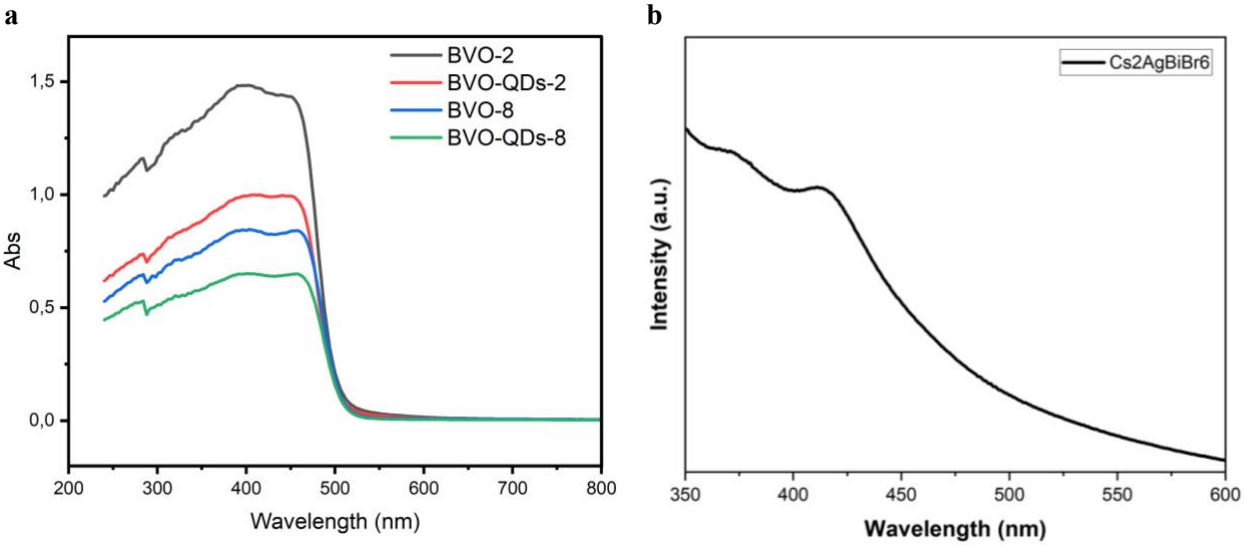

Figure 14: UV-Vis diffuse reflectance spectra (DRS) of (a) BVO-2, BVO-QDs-2, BVO-8, BVO-QDs-8 samples and (b) Cs_2 AgBiBr_6 QDs sample

1.4. FT-IR Analysis

FTIR spectra of pristine $BiVO_4$ and its composites with $Cs_2AgBiBr_6$ were analyzed to determine functional groups and vibrational modes can be seen in Fig. 15. According to previous report[55], vibrations associated with V1 (VO_4) and V3 (VO_4) exhibit absorption at low frequencies, typically below 400–900 cm^{-1}. However, these peaks cannot be observed due to limitation of the used FT-IR

instrument. The peak detected at 1380 cm^{-1} in BVO-2 and BVO-QDs-2 sample belongs to the bending vibration of unreacted NO_3^- group from salt precursor[56]. This result suggests that NO_3^- anions are present in the $BiVO_4$ compound at pH 2. In contrast, there is no significant peak belong to NO_3^- group was found in BVO-8 and BVO-QDs-8 samples.

By the other hand, the small bands at 1600 cm^{-1} and 3650 cm^{-1} are associated with the O-H group, indicating that water might absorb on the oxide surface[56]. In addition, the band around to 2200-2300 cm^{-1} was assigned to the adsorbed atmospheric CO_2 molecules[57].

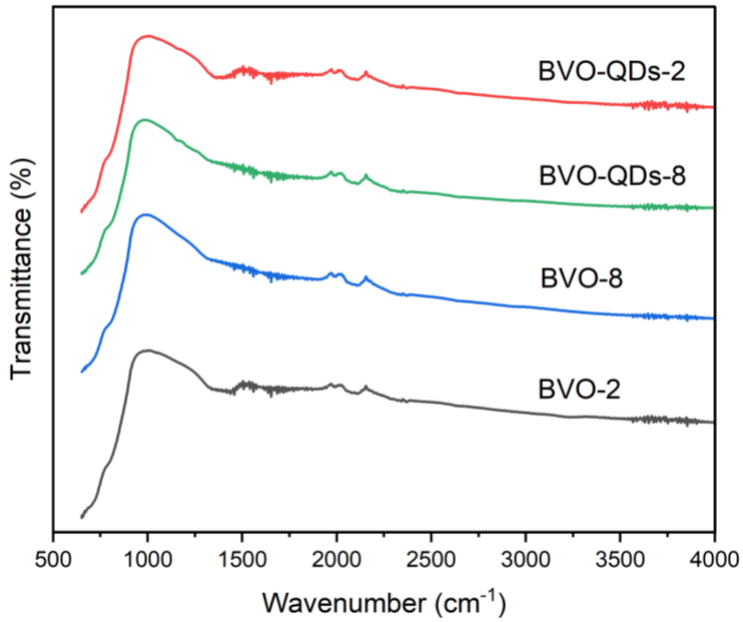

Figure 15: FT-IR spectra of BVO-2, BVO-QDs-2, BVO-8, BVO-QDs-8 samples

1.5. Raman Analysis

Raman scattering spectroscopy serves as a powerful technique for analyzing the structure and bonding within metal-oxide compounds by examining their vibrational properties. Fig. 16 and Table 1 presented Raman spectra and their vibration assignment of BVO and BVO-QDs samples.

Our obtained results are aligned with previous studies. In the monoclinic state of $BiVO_4$, the Raman spectra display six distinct vibrational bands at 210, 327, 367, 637, 702, and 826 cm^{-1}, indicative of the vibrational characteristics of the VO_4 tetrahedron[58]. The appearance of these bands in our BVO-2 and BVO-8 samples confirmed the monoclinic structure of $BiVO_4$. The strong band observed at 828 cm^{-1} is associated with the shorter symmetric V–O stretching mode (A_g), whereas the weaker bands at 702 is attributed to the long (A_g) asymmetric V–O stretching modes, respectively[59]. The symmetric (A_g) and antisymmetric (B_g) bending modes are observed at 369 and approximately 327 cm^{-1},

respectively[58], while the external mode at around 212 and 129 cm^{-1} is generated by the spin and frequency shift of the V–O bond in the VO_4^{3-} group and correspond to the vibration of the crystal lattice[60 61].

For BVO-QDs composite, the $Cs_2AgBiBr_6$ spectra could not be observed from the same measurement conditions. Since there was no signal for the QDs compound was detected, it could not be concluded that our QDs compound was successfully attached to the BVO surface.

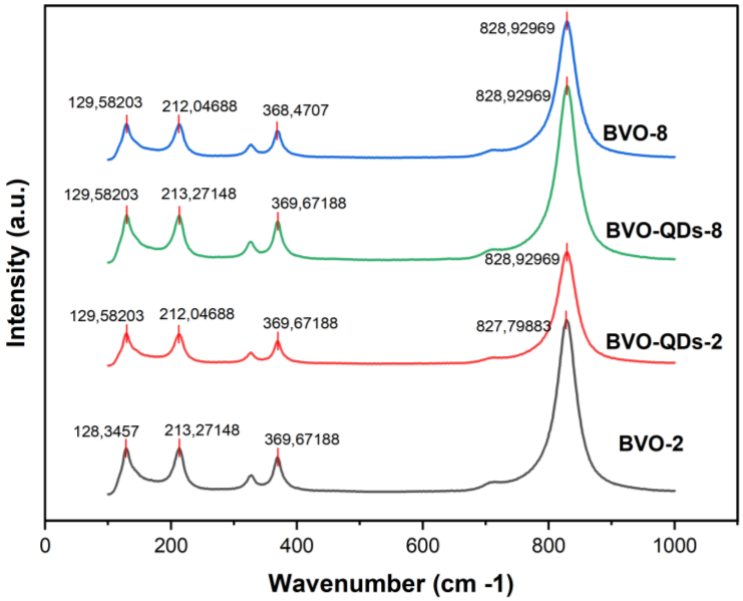

Figure 16: Raman spectra of BVO-2, BVO-QDs-2, BVO-8, BVO-QDs-8 samples

Table 1: Peak assignments of Raman spectra

Assignment	**Raman band positions (cm^{-1})**
ϑ (V-O) short symmetric stretching (A_g)	827-828
ϑ (V-O) long asymmetric stretching (A_g)	702-703
ϑ (V-O) symmetric bending (A_g)	368-369
ϑ (V-O) antisymmetric bending (B_g)	327
Vibration of the crystal lattice	212, 129

1.6. Zeta potential measurement

The particle surface charge has a huge impact on the selectivity of absorbed substances onto the catalytic surface, thus affecting the photochemical reaction process. The effect of fuel and the formation of product gradient significantly influence the driving force behind microswimmer movement. Therefore, the surface charge has a significant effect on the propulsion modes and

behaviors. By applying an electric field to the liquid and observing the migration of the particles to the electrode, the charge carried by the particles can be recorded.

Zeta potential can be used to describe the surface adsorption capacity of oxides, which is influenced by Coulomb forces. Therefore, zeta potentials were measured to examine the surface charge of our samples that were dispersed in ethanol solution. The value of the Zeta potential of all compounds is mentioned in Table 2, indicating that the surface of all samples is positively charged in polar aqueous solution. Moreover, the addition of $Cs_2AgBiBr_6$ QDs increased the number of positive ions of the BVO-2 sample but it did not significantly impact the BVO-8 sample.

Table 2: Zeta potential values of BVO-2, BVO-QDs-2, BVO-8, BVO-QDs-8 samples

Sample	Zeta potential
BVO-2	+ 6.01
BVO-QDs-2	+ 10.14
BVO-8	+ 13.46
BVO-QDs-8	+ 14.57

The surface charge of $BiVO_4$ microrobots change with pH due to the ionization states of surface functional groups and the adsorption of ions from the solution. At low pH, the protonation of surface hydroxyl groups of $BiVO_4$ results in a positive zeta potential on the surface ($BiOH + H^+ \rightarrow BiOH_2{}^+$). BVO-2 has a lower positive zeta potential because fewer positive ions are available for adsorption due to the high concentration of H^+ ions. At high pH, the deprotonation of surface hydroxyl groups occurs ($BiOH \rightarrow BiO^- + H^+$), leading to a negative or less positive surface charge. However, in the presence of basic conditions, $BiVO_4$ surfaces can adsorb more positive ions from the solution, slightly increasing the zeta potential. It can be proposed that BVO-8 exhibits a higher positive zeta potential due to the adsorption of Na^+ ions from the NaOH solution. It can be concluded that the surface charge of metal oxides like $BiVO_4$ is highly pH dependent. The adsorption/desorption equilibrium of ions from the solution is affected by the ionization of surface functional groups (e.g., hydroxyl groups) that change with the pH.

2. FORMATION MECHANISM

Table 3: The behaviour of precursor ions at different pH

	Bismuth Ions (Bi^{3+}) behavior	**Vanadium Species (VO_4^{3-}) behavior**
Acidic Conditions (pH 2 - 4):	At low pH, Bi^{3+} ions remain relatively stable in solution. There is minimal hydrolysis, meaning that Bi^{3+} ions stay in their ionic form. The formation of $BiVO_4$ in acidic conditions tends to be straightforward as the Bi^{3+} ions are readily available to react with vanadate ions (VO_4^{3-}).	VO_4^{3-} ions tend to convert into vanadyl (VO^{2+}) and other polyvanadate species like HVO_4^{2-}, $H_2VO_4^-$ and H_3VO_4 For example, at low pH: $VO_4^{3-} + H^+ \rightleftharpoons HVO_4^{2-}$, $HVO_4^{2-} + H^+ \rightleftharpoons H_2VO_4^-$ $H_2VO_4^- + H^+ \rightleftharpoons H_3VO_4$ These species have different reactivities compared to VO_4^{3-} and can influence the formation and phase composition of $BiVO_4$.
Neutral to Basic Conditions (pH 5 - 8):	As pH increases, Bi^{3+} ions begin to hydrolyze, forming various hydroxide species such as $Bi(OH)^{2+}$, $Bi(OH)_3$ and BiO^+. For example, at pH ~ 5: $Bi^{3+} + H_2O \leftrightarrow Bi(OH)^{2+} + H^+$ $Bi(OH)^{2+} + H_2O \leftrightarrow Bi(OH)_2^+ + H^+$ At higher pH ~ 7-8: Bi^{3+} ions can precipitate as $Bi(OH)_3$ or $BiO(OH)$, which are less soluble and can hinder the formation of $BiVO_4$. These hydroxides and oxyhydroxides can act as nucleation sites or interfere with the uniform growth of $BiVO_4$ crystals.	In neutral to basic conditions, VO_4^{3-} remains relatively stable as a vanadate ion. This stability supports the straightforward formation of $BiVO_4$. since VO_4^{3-} is the primary species reacting with Bi^{3+} ions. However, in highly basic conditions, there can be competition between VO_4^{3-} and hydroxyl ions (OH^-), potentially affecting the overall reaction dynamics and product purity.

Tables 3 summarizes the effect of pH on the Bi^{3+} and VO_4^{3-} precursors in terms of solubility, speciation, and precipitation behavior of the precursors, which in turn impacts the final product's phase purity and morphology. The formation mechanism at different pH of $BiVO_4$ is explained in Supporting Information.

From the obtained results, we can propose a hypothesis on the formation mechanism of $BiVO_4$. For the acidic $Bi(NO_3)_3$ solution, the main existing forms of Bi sources are Bi^{3+}, $Bi(OH)_2{}^+$, $Bi(OH)^{2+}$ and BiO^+, and the primary form of the V source changes sequentially into $VO_2{}^+$ and $VO_3{}^-$ [62]. Since there was no detection of V_2O_5 oxide in all measured samples, the formation of NH_4VO_3 might not be completed or it was fully reacted with OH^- from NaOH to form $VO_3{}^-$.

When the dropwise of $NaVO_3$ in NH_3 is added to $Bi(NO_3)_3 \cdot 5H_2O$ in HNO_3, the acid–base and the precipitation reactions will take place and lead to the change in pH value of the reaction system. It is suggested that V source exists mainly in the $VO_2{}^+$ form and $VO_3{}^-$ at pH 2 and 8, respectively[64]. In our study, the observed pH after mixing Bi^{3+} and V^{5+} precursors are around 0.85, which reveals that $VO_2{}^+$ ion is the main V source. The pH of the mixture was adjusted by NaOH to obtain the value of 2 and 8. The formation of $VO_2{}^+$ and H^+ ions explain the positively zeta potential value of the BVO-2 sample. In the case of the BVO-8 sample, as the adding of OH^- ions, the reaction (*) may slowly occur during the hydrothermal process and dominate the whole process, thus giving an increase in H^+ ion. This led to the positive zeta potential value of the BVO-8 sample.

3. CHARACTERIZATION OF MOTION

When aqueous dispersions of $BiVO_4$ and its composite microrobots are illuminated with visible light, it generates electron-hole pairs within the particles. This photogeneration produces various ions and chemical species that diffuse at different rates, thus forming an asymmetrical chemical gradient around the particles. This gradient triggers their ballistic motion through phoretic mechanisms. Propulsion of the microswimmers is achieved by illuminating them with visible light and intensity of 30 mW/cm^2. The swimming behavior is tracked for 10 seconds. The swimmers are tested under deionized water without the presence of any additional fuel.

It can be observed that the microswimmers are actively propelled by light, indicating that the movement is influenced by light but not a result of active Brownian motion only, as shown in Fig. 17. Two mechanisms can be considered for the swimming mechanisms of the microswimmers under visible light. First, the microswimmers swim due to a photocatalytic water splitting reaction[65]. When they absorb light, they create energy-rich electrons which can be discharged through redox reactions with their environment, thus breaking down water into photogenerated products. The second propulsion mechanism of our microrobots is based on light-induced self-electrophoresis, which results from asymmetric distribution of ions. The variation in ionic concentration will propel the microswimmers[66].

From the obtained results, the addition of $Cs_2AgBiBr_6$ QDs enhanced the movement velocity of the bare $BiVO_4$. This can be explained by an increase in proton concentration gradient on the surface of the BVO-QDs microswimmers, which was demonstrated through zeta potential value. A better charge transfer to the surface generated a greater number of electrons on the surface, leading to an increased self-electrophoresis of the particles. Therefore, the BVO-QDs microswimmers would move at higher speeds.

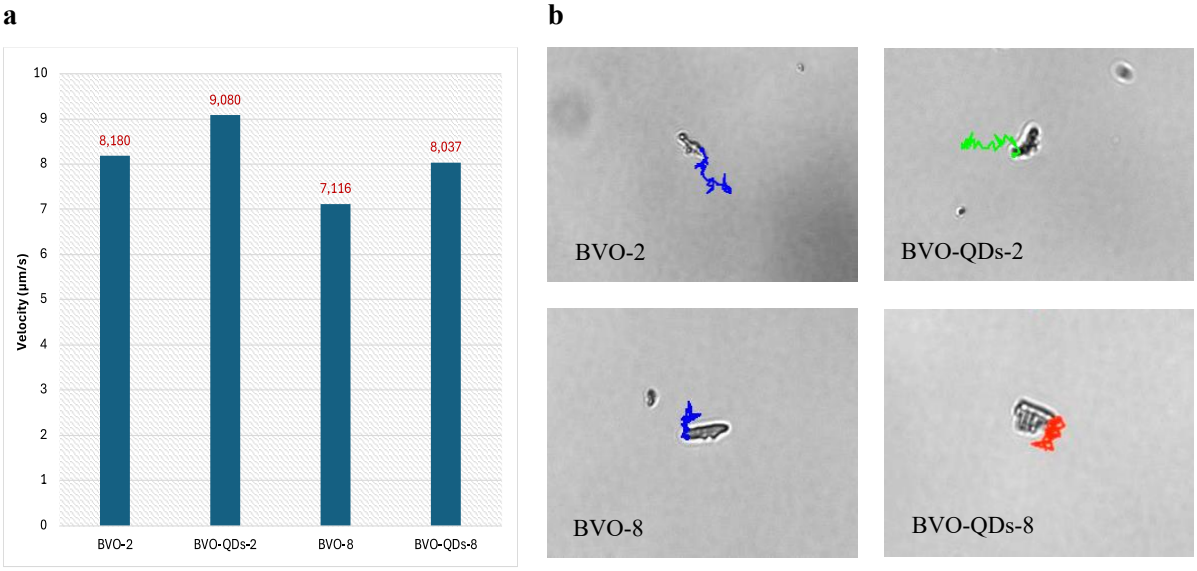

Figure 17: (a) Average (N=10) mean speed in μm/s and (b) Snapshot images of a BVO-2, BVO-QDs-2, BVO-8 and BVO-QDs-8 microswimmers placed in an aqueous environment under visible light exposure (left to right)

4. ACTIVE PHOTOCATALYTIC DEGRADATION

The environmental remediation of antibiotics and dyes has been widely studied. . Traditional antibiotic degradation systems often face challenges with poor micro-mixing and mass transfer within the solution, which limits the degradation rate. Active matter and microswimmers can enhance the micro-mixing of the solutes as they move through the solution, improving active sites and pollutant contact and thus speeding up the degradation process.

Like many light-driven photocatalytic micromotors, $BiVO_4$ can oxidize organic pollutants under light exposure. Its photocatalytic activity enhancement can be achieved by coupling $BiVO_4$ with another photoactive material. This combination can promote electron-hole pair separation and delay recombination time, thus leading to greater photocatalytic efficiency. In this part, we will confirm an increase in photocatalytic activity of BVO-QDs microswimmers, which is demonstrated by the higher

degradation efficiency of three antibiotics: Azithromycin, Erythromycin, and Clarithromycin (Fig. 18).

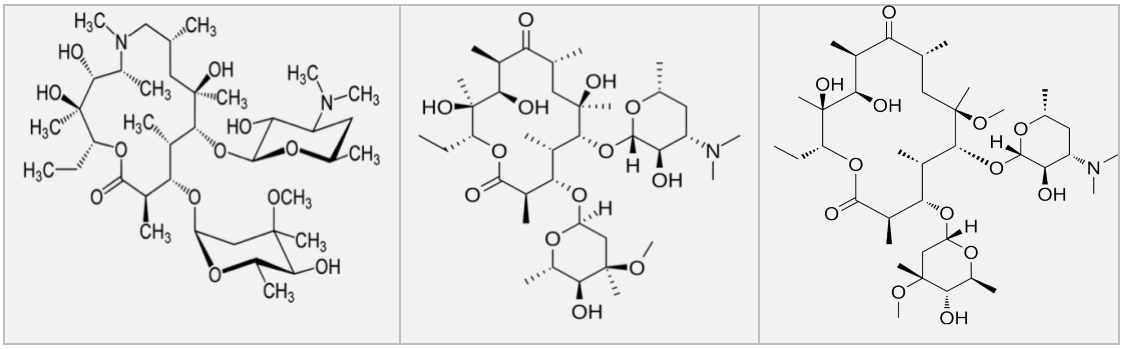

Figure 18: Chemical structure of Azithromycin, Erythromycin and Clarithromycin (from left to right)

Fig. 19a presents the degradation profile of Azithromycin by BVO and BVO-QDs microswimmers under visible light irradiation. We demonstrated that the BVO-QDs microswimmers exhibit enhanced photocatalytic activity in compare with the bare BVO. The maximum degradation percentages were achieved at 90 min by applying the BVO-QDs-2 microrobots, at which almost 72% of the antibiotics were degraded within 90 min of light exposure, followed by the BVO-QDs-8 sample with 69% of treatment efficiency. On the other hand, the BVO-2 sample exhibited moderate catalytic activity since about 59% of antibiotics were degraded after 90 min. Even though the BVO-8 sample exhibited much less efficient movement compared to the BVO-2 sample, its photocatalytic activity was slightly better as about 63% of Azithromycin was treated. Drug degradation was slow due to the lower driving force facilitating the movement of microrobots in the solution, which limiting the approach of drug molecular to the catalyst surfaces and active sites. After this period, the degradation rate increased significantly due to the enhancement of the diffusion effect, which requires sufficient exposure time to boost the microrobot's movement throughout the solution, thus facilitating more efficient degradation reactions.

The same degradation rate was observed in the degradation profile of Erythromycin; however, the degradation efficiency was in a different order: BVO-QDs-2 < BVO-2 < BVO-8 < BVO-QDs-8 (Fig. 19b). The degradation results revealed the proficiency of BVO-QDs-8 sample toward Erythromycin antibiotics, at which 72% of the pollutant were degraded after 90 min. In contrast, less than 50% of Erythromycin were degraded using the other 3 microrobots despite of their greater movement behavior in compare with BVO-QDs-8 sample.

A different degradation behavior was observed toward the degradation of Clarithromycin by BVO and BVO-QDs microrobots under visible light irradiation (Fig. 19c). Over 50% antibiotics were

degraded by BVO-8 and BVO-QDs-8 sample in the first 30 min, which was much higher than the same treatment toward Azithromycin and Erythromycin. After 90 min of treatment, the degradation efficiencies of BVO-2, BVO-QDs-2, BVO-8 and BVO-QDs-8 samples were 51%, 50%, 75% and 80%, respectively. The BVO-QDs-8 compound exhibited the highest photocatalytic activity toward Clarithromycin.

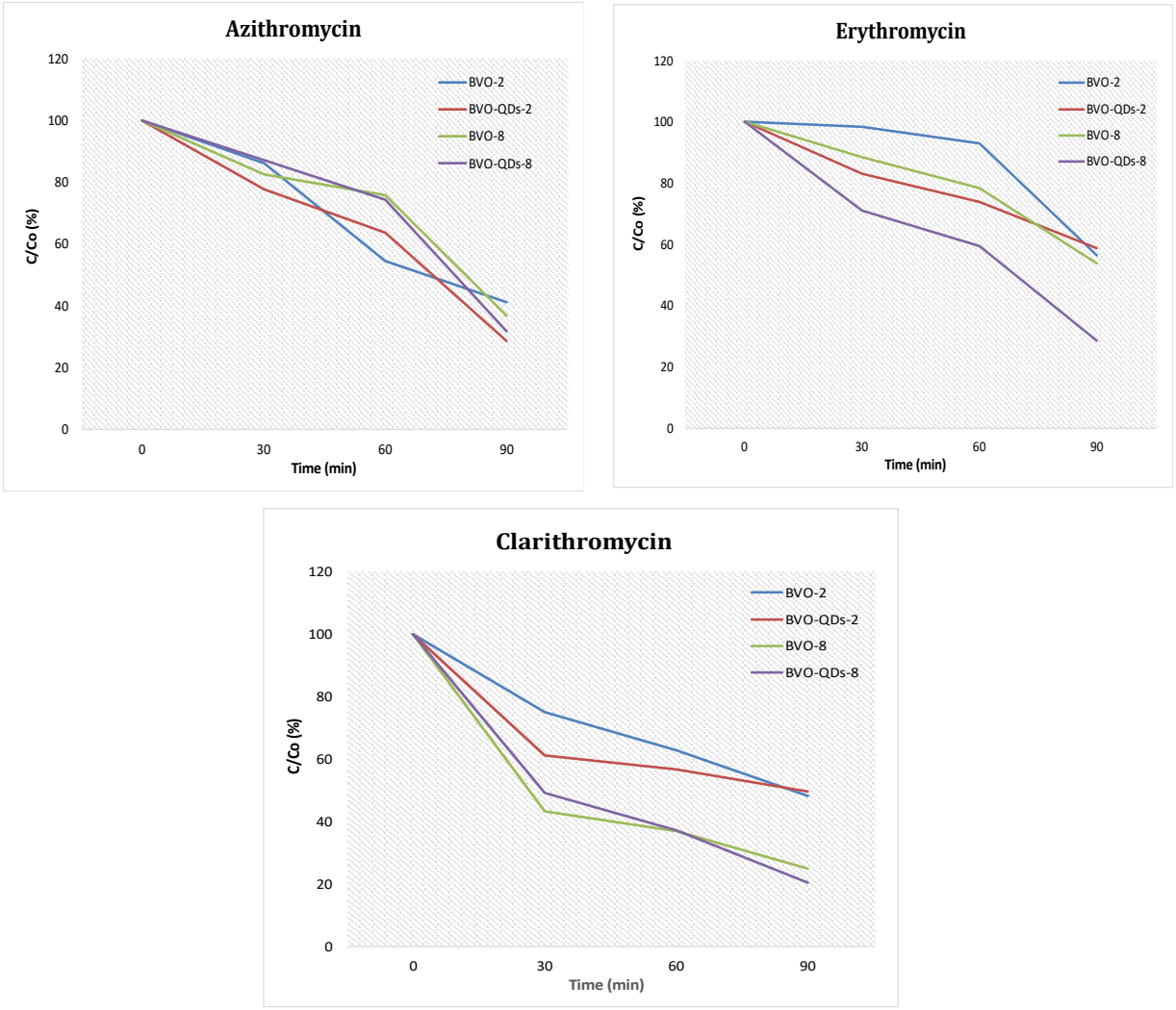

Figure 19: Photocatalytic degradation of Azithromycin, Erythromycin and Clarithromycin

From the obtained results, it can be suspicious that both movement behaviors and the charge surface of microrobots affect their photocatalytic activity towards antibiotics. When the photocatalyst particles are dispersed in a substrate solution, the surface charge can not only affect the stability of the system but also influence the adsorption or interaction of substrates and catalyst surface, thus impacting photocatalytic activity. Although the higher movement of microswimmers might play some roles, the charged surface is the main factor for the catalytic activity improvement.

5. POSSIBLE DEGRADATION MECHANISM

In general, photocatalytic reaction takes place by the following steps:

(1) Adsorption of the organic compound onto the catalyst surface

Firstly, antibiotic molecules are adsorbed onto the surface of the $BiVO_4$ microrobots. The adsorption efficiency is affected by the surface charge of the microrobots and the charge of the antibiotic molecules. In our study, the higher zeta potential value of synthesized compounds leads to the better adsorption of antibiotics on the catalyst surface because the studied antibiotics are negatively charged due to the free electron pair of the N atom. Based on this reason, the adsorption efficiency can be ranked as follows BVO-QDs-8 > BVO-8 > BVO-QDs-2 > BVO-2

(2) Generation of reactive oxygen species (ROS)

Under visible light irradiation, BVO and BVO-QDs microrobots absorb light energy and excite electrons from the valence band to the conduction band, creating electron-hole pairs. The photoexcited electrons (e^-) and holes (h^+) participate in redox reactions to generate ROS, which are mainly hydroxyl radicals (•OH), superoxide anions ($O_2^{\bullet-}$), and hydrogen peroxide (H_2O_2). These radicals and compounds are the active species for the pollutant degradation process.

$$h^+ + H_2O \rightarrow \bullet OH + H^+$$

$$e^- + O_2 \rightarrow O_2^{\bullet-}$$

$$O_2^{\bullet-} + H^+ \rightarrow H_2O_2$$

$$H_2O_2 \rightarrow 2 \bullet OH \quad \text{(light irradiation)}$$

(3) Reaction with the antibiotics

The hydroxyl radical ($OH^{\cdot}$) is the main reactive species driving the degradation process. The degradation reactions involve the hydroxylation of the aromatic ring through an electrophilic attack by the $OH^{\cdot}$, cleavage of C-O, C-N, or S-N bonds[67]. •OH radicals can also go for electrophilically attack to the aromatic rings and other susceptible sites in the antibiotic molecules, leading to ring opening and subsequent degradation. The possible sites of $OH^{\cdot}$ electrophilic attack is illustrated in Fig. 20. The degradation pathway of each compound can be proposed:

- Azithromycin: The attack primarily targets the lactone ring and desosamine sugar moiety, breaking down the macrolide structure.
- Erythromycin: Like azithromycin, the hydroxyl radicals attack the lactone ring, leading to the breakdown of the antibiotic.
- Clarithromycin: The degradation involves breaking the ether linkages and the lactone ring, resulting in smaller fragments.

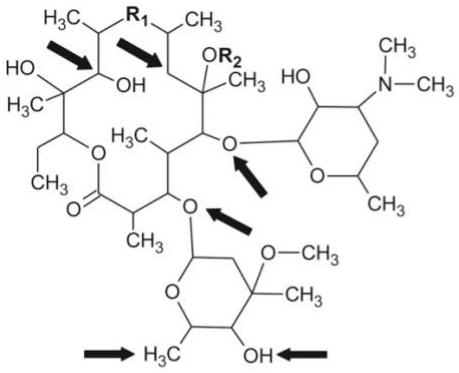

$R_1 = CO$	$R_2 = H$	Erythromycin
$R_1 = CO$	$R_2 = CH_3$	Clarythromycin
$R_1 = N(CH_3)CH_2$	$R_2 = H$	Azithromycin
$R_1 = NOCH_2O(CH_2)_2OCH_3$	$R_2 = H$	Roxithromycin

Figure 20: Possible sites of $OH^{\cdot}$ radical attack on macrolide molecule[52]

(4) Desorption of products from the catalyst surface

The degradation products desorb from the surface of the microrobots and empty the active sites for further catalytic reactions. This step allows the continuous activity of the microrobots for antibiotics degradation.

There are several factors that influence the degradation efficiency. Firstly, the surface charge of the compound plays an important role in determining the adsorption effectiveness of antibiotics on catalyst surface. BVO-8 and BVO-QDs-8 samples with higher positive zeta potential values showed better interaction with antibiotics, thus could enhance the catalytic degradation process. Moreover, the photocatalytic activity of microrobots also proofed and improvement in catalytic activity. From the obtained results, it can be proposed that the presence of $Cs_2AgBiBr_6$ QDs improve the catalytic activity of $BiVO_4$ compound by delaying electron-hole pairs recombination. Finally, the movement behavior also plays some part in enhancing the degradation efficiency. The enhanced movement of microrobots under light improves micro-mixing and contact with antibiotic molecules, thus facilitating a better degradation process. This can be explained for the higher photocatalytic efficiency of BVO-QDs-2 as the adding of QDs not only improved charge separation but also enhanced the movement under light.

Chapter 4: Conclusion

Light-driven microrobots represent a kind of green technology in environmental remediation. As one of the most abundant energy sources, light serves as a promising stimulus for the propulsion of microswimmers, allowing remote control, superposition, and spatial as well as temporal manipulation. Thanks to these benefits, light-driven microswimmers attract more and more attention in the development of microswimmer technology. In this thesis, we have explored the fabrication of visible-light-driven $BiVO_4$-based microswimmers, their motion behaviors, and photocatalytic activity towards some emerged pollutants.

Bismuth vanadate ($BiVO_4$) is an effective visible light-driven catalyst that has been designed as a functional microrobot. $BiVO_4$ can be produced in various shapes using easy, solvent-free, and one-step synthesis hydrothermal methods. The structure and physical properties including surface area, particle size, and surface charge can be simply altered by adjusting the pH value. Both NaOH and NH_3 can be used to adjust pH, but they have different mechanisms and implications on the synthesis process. Among all samples, the fishbone-shaped $BiVO_4$ microswimmers with an interesting surface charge property have been studied and developed. $Cs_2AgBiBr_6$ QDs were fabricated along with fishbone-shaped $BiVO_4$, and the composite showed an enhancement in surface charge, movement velocity and catalytic activity. The propulsion of these synthesized light-driven microswimmers might be due to either water splitting reaction or the transfer of electrons from the $BiVO_4$ side to the $Cs_2AgBiBr_6$ side, resulting in the fluid flow that propels the microswimmers. The microswimmers could swim in both UV and visible light, making them as promising candidates for wide-range applications.

We also explore the use of $BiVO_4$ as a highly effective photocatalyst for developing efficient light-driven microswimmers. The degradation experiments for Azithromycin, Erythromycin, and Clarithromycin under visible light irradiation demonstrated that our prepared microrobots exhibit excellent photocatalytic activity without the need for continuous solvent mixing during treatment. Overall, the best photocatalytic activity was awarded to the BVO-QDs-8 sample. Its achieved degradation percentages of 69% for Azithromycin, 72% for Erythromycin and 80% for Clarithromycin surpassed the based $BiVO_4$ compound, demonstrating the superiority of the composites.

This study provides a new perspective on the fabrication of microrobots for water remediation, highlighting advantages such as eco-friendly fabrication, low cost and easily scalable. Despite the

significant advancements made in the propulsion of light-driven microswimmers, the lack of movement control limits the microrobots in practical applications. Therefore, the swarm control study is demanded to push light-driven microswimmers towards practical applications. As microrobots exhibit phototactic behavior that allows them to move toward or away from light depending on their zeta potential, optical control can be applied to navigate the collective behavior of microrobots. Another method is magnetic control, which is the most common method to direct the movement of microswimmers. It can be achieved by applying an extra magnetic layer or adding iron-based nanoparticles to microrobots' surface, allowing their movement to be controlled using a magnet. This method can also allow the recovery of materials, which is advantageous for larger-scale applications.

Chapter 5: Experimental section

A. GENERAL INFORMATION

Bismuth (III) nitrate pentahydrate ($Bi(NO_3)_3 \cdot 5H_2O$, 98 %), nitric acid (HNO_3, 65 %), ammonia solution (NH_3, 35%), sodium metavanadate ($NaVO_3$, 96 %), sodium hydroxide (> 97%) was obtained from Sigma-Aldrich (Merck, Germany). $Cs_2AgBiBr_6$ was given by the Palomares's research group. Azithromycin, Erythromycin and Clarithromycin (> 98%) were also obtained from Sigma-Aldrich (Merck, Germany).

B. SYNTHESIS OF $BiVO_4$ AND $BiVO_4-Cs_2AgBiBr_6$QDs MICROROBOTS

The preparation procedure was illustrated in Figure 21.

B.1. Synthesis of $BiVO_4$ microrobots

Different shape of $BiVO_4$ microrobots were prepared by a simple solvent-free hydrothermal reaction as follows. $Bi(NO_3)_3 \cdot 5H_2O$ (1 mmol) was dissolved in a 4M HNO_3 solution (20 mL) and marked as solution A. An additional solution of $NaVO_3$ (1 mmol) was prepared in 20 mL of 4M basic solution (NH_3 or NaOH) and marked as solution B. Both solutions were stirred for 20 min at room temperature, then solution B was then added dropwise into the solution A. The resulting yellow solution underwent pH adjustment before being transferred into a 50 mL Teflon-lined stainless-steel autoclave reactor and heated at 180°C for 10h. The collected precipitate was washed and centrifugated with ethanol and distilled water four times. The clean samples were dried in an oven at 80°C overnight and stored properly.

B.2. Synthesis of $Cs_2AgBiBr_6$ QDs

This work was performed by Shence Zhang from Palomares's research group (ICIQ, Spain). The procedures are as follow:

- Synthesis of Cs-Oleate: 0.20 mmol Cs_2CO_3 (100mg), 5 ml ODE and 0.3 ml OA were loaded into a 25mL 2-neck round-bottom flask, kept in vacuum for 1h at 120℃, and then under N_2 environment was heated to 150℃ until the formation of Cs-oleate.
- Synthesis of $Cs_2AgBiBr_6$ NCs: In a typical synthesis, 0.20 mmol $BiBr_3$ (90mg), 0.20mmol $AgNO_3$ (34 mg), 2 mL of OA, 2 mL of OLAM, and 8 mL of ODE were loaded into a 50 mL 3-neck round-bottom flask and dried under vacuum at 120°C for 1h. Subsequently, the temperature was increased to 200°C under N_2, and 2 ml Cs-oleate was swiftly injected. After 5 seconds, the reaction mixture was immediately cooled down in an ice–water bath. Then, the resulting mixture was centrifuged at 8000 rpm for 5 min. The supernatant was discarded, and the precipitate was dispersed in chloroform.

- Washing process of $Cs_2AgBiBr_6$ NCs: Half volume of absolute ethanol was added into the obtained solution and shook for 30-60 seconds. Afterwards, the mixture was separated by centrifuging at 12,000 rpm for 5 min, and the yellow precipitates were collected by discarding supernatant. This process was repeated twice.

B.3. Synthesis of $BiVO_4-Cs_2AgBiBr_6$ composite

2 mg of $Cs_2AgBiBr_6$ QDs and 200 mg of $BiVO_4$ microrobots were mixed and dispersed in 10 mL Milli–Q H_2O before mixing with each other. The mixture was stirred for 8h then dried at 60ºC in 2 days.

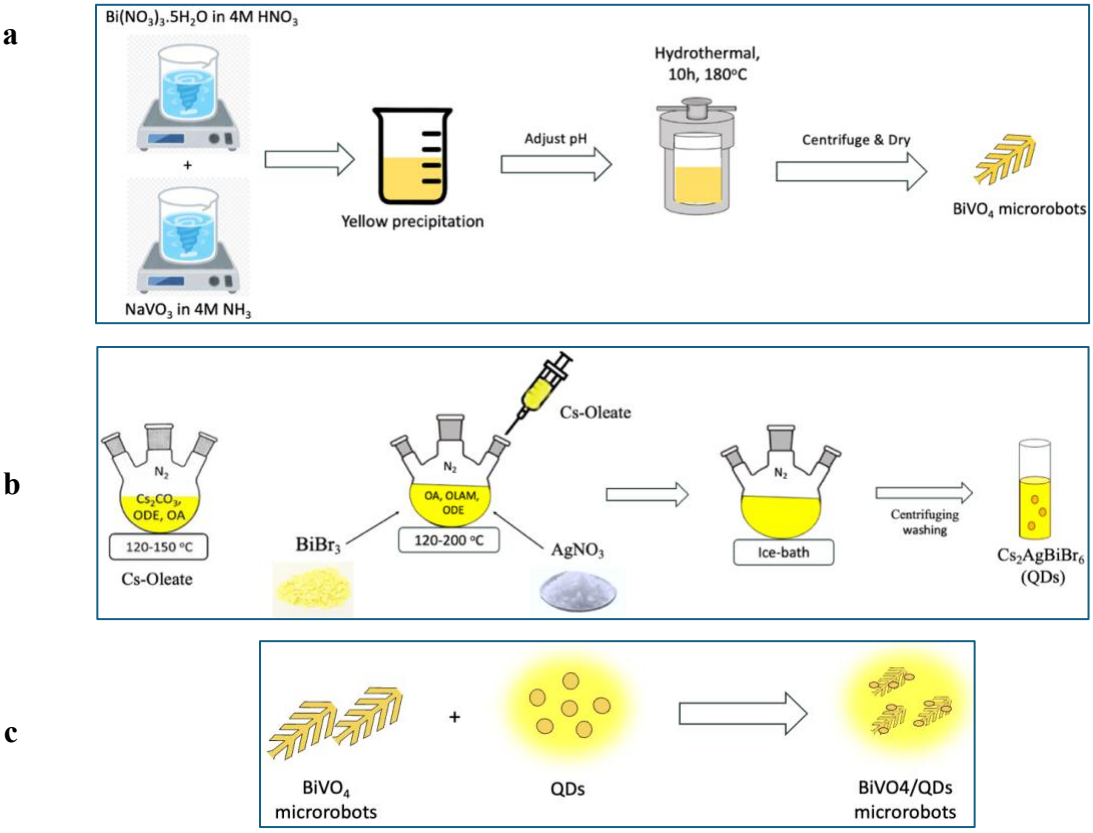

Figure 21: The preparation of (a) $BiVO_4$, (b) $Cs_2AgBiBr_6$ QDs (b) and (c) $BiVO_4$-Cs_2 $AgBiBr_6$ composited microrobots

C. MORPHOLOGICAL AND STRUCTURAL CHARACTERIZATION OF THE MICROROBOTS

The morphology of our microrobots were obtained using a FE-SEM Quanta 600 from FEI company, uses an electron beam to form the image, equipped with an EDX (URV, Spain). The morphology of $BiVO_4 - Cs_2AgBiBr_6$ QDs composites was figured out by HR-TEM JEOL F200 instrument,

incorporates a high energy resolution EDX detector and complemented with a CMOS-based Gatan OneView camera of 4096 by 4096 pixels to capture images and diffraction patterns (URV, Spain).

X-ray diffraction measurements (XRD) were made using a Bruker-AXS D8-Advance diffractometer with vertical theta-theta goniometer, incident- and diffracted-beam Soller slits of 2.5º, a fixed 0.5º receiving slit and an automatic Air-scattering knife on the sample surface (URV, Spain). The angular 2θ range was between 5 and 80º. The data were collected with an angular step of 0.02º at a step/time of 0.5s. Cukα radiation was obtained from a copper X-ray tube operated at 40 kV and 40 mA. Diffracted X-rays were detected with a PSD detector LynxEye-XE-T with an opening angle of 2.94º. Sample was deposited on a low-background support (Si (510)). The diffractograms were interpreted with the software DIFFRAC.EVA 6.0 from BRUKER.AXS and the database PDF-2 release 2022 from ICDD (International Center for Diffraction Data).

Raman spectra were obtained by the Raman microscope Renishaw InVia (URV, Spain). Spectrophotometer equipped with three diffraction gratings of 2400 lines/mm, 1200 lines/mm and 600 lines/mm, it has three available lasers of 514 nm, 633 nm and 785 nm of wavelength. Samples were excited with a 514 nm laser source. Measurements were performed at 25 mW laser power intensity and integration times of 2.0 s. All the Raman spectra excited with the same wavelength directly compared in the following sections were recorded at similar conditions.

FT-IR spectra were recorded for all samples using a pressed mixture of $BiVO_4$ powders and KBr formed into pellets (mass ratio of $BiVO_4$: KBr is 1:2). This analysis was conducted with a spectrometer within the range of 4000–600 cm^{-1}. The obtained reflectance spectra were converted to absorbance by using the Kubelka–Munk function. where α is the absorbance, R is the measured reflectance.

$$\alpha \approx F(R) = \frac{(1-R)^2}{2R}$$

The optical bandgap can be estimated by extrapolating the onset of absorption to the wavelength axis in the Tauc plot. This relationship is described by the Tauc equation, where α is the absorption coefficient, $h\nu$ is the photon energy, A is a constant, E_g is the bandgap energy, and n is an exponent that depends on the type of transition.

$$\alpha h\nu = A(h\nu - E_g)^n$$

The surface charge of microrobots was measured as zeta potential (mV) using the Zetasizer Ultra (Malvern Panalytical, URV, Spain). The concentration of the catalysts was 0.5 mg/cm^{-1} in Ethanol solution (96%).

D. MOTION BEHAVIOR OF MICROROBOTS

The light-powered motion behavior of microrobots in water was observed and recorded using the Nikon TE 2000E confocal scanning laser microscope with a 40x objective lens, coupled to HBO100 mercury lamp used as a light source to visualize fluorescent samples; and the transmitted light for bright field and for differential interference contrast (URV, Spain). All experiments were carried out without the use of any surfactant and fuel. Briefly, a microrobot aqueous suspension was dropped on a glass slide. Then, the microrobots were powered by natural light. The videos were recorded at 3.7 fps using NIS Elements Advanced Research and analyzed through Fiji software to achieve microrobots' trajectories and measure their speed.

E. PHOTOCATALYTIC DEGRADATION OF ANTIBIOTICS

The photocatalytic degradation ability of microrobots was evaluated through the degradation of antibiotics under visible light. In detail, 3 mg of microrobots were added to 3 mL of antibiotics (10 ppm) in 6 mL of glass container. The container was irradiated under visible light source for 0, 30, 60 and 90 min. After the photocatalytic experiments, the solution was filtered using 0.22 μm membrane filter to separate the solution from the microrobots for further analysis.

The remaining concentration of antibiotics were analyzed on a Thermo Scientific™ Orbitrap Exploris mass spectrometer with a HESI interface, in line with Vanquish UHPLC Liquid Chromatograph. An Acquity UPLC BEH C18 column (2.1 x 150 mm x 1.7 mm) provided by Waters was used at temperature and flow of 40ºC and 0.4 mL/min, respectively. H_2O 0.1% formic acid (A) and ACN 0.1% formic acid (B) were used for gradient elution, and injection volume was 5 ml. The optimized gradient was programmed as follows: starting with 25% B, the gradient remained isocratic for 1 min, then increased within 1 min to 90% B and stayed constant for 1 min, then decreased within 1 min to 75%B. For re-equilibration, the gradient was changed to starting conditions within 0.5 min and held constant for 2 min. The total run time was 6.5 min. For MS detection, heated electrospray ionization settings were set in positive ionization mode as follows: source voltage, 4.0 kV; vaporizer temperature, 300ºC; sheath gas (N_2) flow rate, 40 a.u., auxiliary gas (N_2) flow rate, 10 a.u., sweep gas (N_2) flow rate, 0 a.u.; s-lens rf level, 70%; SCAN-mode; resolution, 60 000 (at m/z 200), maximum injection time, 200 ms. Xcalibur 4.4 software (Thermo Scientific) was used for LC/MS instrument control and data processing. The photocatalytic degradation efficiency was calculated using equation below, where C and C_0 represent the absorbance of the residual solution and the initial solution.

$$\eta\ (\%) = \frac{C_0 - C_t}{C_0} \times 100\%$$

Reference

(1) Nguyen, P. Y.; Carvalho, G.; Reis, M. A. M.; Oehmen, A. A Review of the Biotransformations of Priority Pharmaceuticals in Biological Wastewater Treatment Processes. *Water Research* **2021**, *188*, 116446. https://doi.org/10.1016/j.watres.2020.116446.

(2) Urso, M.; Ussia, M.; Pumera, M. Smart Micro- and Nanorobots for Water Purification. *Nat Rev Bioeng* **2023**, *1* (4), 236–251. https://doi.org/10.1038/s44222-023-00025-9.

(3) Wang, J. Can Man-Made Nanomachines Compete with Nature Biomotors? *ACS Nano* **2009**, *3* (1), 4–9. https://doi.org/10.1021/nn800829k.

(4) Yuan, K.; Bujalance-Fernández, J.; Jurado-Sánchez, B.; Escarpa, A. Light-Driven Nanomotors and Micromotors: Envisioning New Analytical Possibilities for Bio-Sensing. *Microchim Acta* **2020**, *187* (10), 581. https://doi.org/10.1007/s00604-020-04541-y.

(5) Jurado-Sánchez, B.; Pacheco, M.; Maria-Hormigos, R.; Escarpa, A. Perspectives on Janus Micromotors: Materials and Applications. *Applied Materials Today* **2017**, *9*, 407–418. https://doi.org/10.1016/j.apmt.2017.09.005.

(6) Walther, A.; Müller, A. H. E. Janus Particles: Synthesis, Self-Assembly, Physical Properties, and Applications. *Chem. Rev.* **2013**, *113* (7), 5194–5261. https://doi.org/10.1021/cr300089t.

(7) Mim, J. J.; Hasan, M.; Chowdhury, M. S.; Ghosh, J.; Mobarak, M. H.; Khanom, F.; Hossain, N. A Comprehensive Review on the Biomedical Frontiers of Nanowire Applications. *Heliyon* **2024**, *10* (8), e29244. https://doi.org/10.1016/j.heliyon.2024.e29244.

(8) Koleoso, M.; Feng, X.; Xue, Y.; Li, Q.; Munshi, T.; Chen, X. Micro/Nanoscale Magnetic Robots for Biomedical Applications. *Materials Today Bio* **2020**, *8*, 100085. https://doi.org/10.1016/j.mtbio.2020.100085.

(9) Wang, Y.; Chen, J.; Su, G.; Mei, J.; Li, J. A Review of Single-Cell Microrobots: Classification, Driving Methods and Applications. *Micromachines* **2023**, *14* (9), 1710. https://doi.org/10.3390/mi14091710.

(10) Xu, L.; Mou, F.; Gong, H.; Luo, M.; Guan, J. Light-Driven Micro/Nanomotors: From Fundamentals to Applications. *Chem. Soc. Rev.* **2017**, *46* (22), 6905–6926. https://doi.org/10.1039/C7CS00516D.

(11) Chen, C.; Karshalev, E.; Guan, J.; Wang, J. Magnesium-Based Micromotors: Water-Powered Propulsion, Multifunctionality, and Biomedical and Environmental Applications. *Small* **2018**, *14* (23), 1704252. https://doi.org/10.1002/smll.201704252.

(12) Yang, W.; Wang, X.; Wang, Z.; Liang, W.; Ge, Z. Light-Powered Microrobots: Recent Progress and Future Challenges. *Optics and Lasers in Engineering* **2023**, *161*, 107380. https://doi.org/10.1016/j.optlaseng.2022.107380.

(13) Eskandarloo, H.; Kierulf, A.; Abbaspourrad, A. Light-Harvesting Synthetic Nano- and Micromotors: A Review. *Nanoscale* **2017**, *9* (34), 12218–12230. https://doi.org/10.1039/C7NR05166B.

(14) Guix, M.; Mayorga-Martinez, C. C.; Merkoçi, A. Nano/Micromotors in (Bio)Chemical Science Applications. *Chem. Rev.* **2014**, *114* (12), 6285–6322. https://doi.org/10.1021/cr400273r.

(15) Guix, M.; Weiz, S. M.; Schmidt, O. G.; Medina-Sánchez, M. Self-Propelled Micro/Nanoparticle Motors. *Part & Part Syst Charact* **2018**, *35* (2), 1700382. https://doi.org/10.1002/ppsc.201700382.

(16) Mou, F.; Li, Y.; Chen, C.; Li, W.; Yin, Y.; Ma, H.; Guan, J. Single-Component TiO_2 Tubular Microengines with Motion Controlled by Light-Induced Bubbles. *Small* **2015**, *11* (21), 2564–2570. https://doi.org/10.1002/smll.201403372.

(17) Wang, Y.; Tu, Y.; Peng, F. The Energy Conversion behind Micro-and Nanomotors. *Micromachines* **2021**, *12* (2), 222. https://doi.org/10.3390/mi12020222.

(18) Hong, Y.; Velegol, D.; Chaturvedi, N.; Sen, A. Biomimetic Behavior of Synthetic Particles: From Microscopic Randomness to Macroscopic Control. *Phys. Chem. Chem. Phys.* **2010**, *12* (7), 1423–1435. https://doi.org/10.1039/B917741H.

(19) Zhou, D.; Zhuang, R.; Chang, X.; Li, L. Enhanced Light-Harvesting Efficiency and Adaptation: A Review on Visible-Light-Driven Micro/Nanomotors. *Research* **2020**, *2020*, 2020/6821595. https://doi.org/10.34133/2020/6821595.

(20) Mallick, A.; Roy, S. Visible Light Driven Catalytic Gold Decorated Soft-Oxometalate (SOM) Based Nanomotors for Organic Pollutant Remediation. *Nanoscale* **2018**, *10* (26), 12713–12722. https://doi.org/10.1039/C8NR03534B.

(21) Tang, X.; Li, Y.; Liu, X.; Liu, D.; Chen, Z.; Arai, T. Vision-Based Automated Control of Magnetic Microrobots. *Micromachines* **2022**, *13* (2), 337. https://doi.org/10.3390/mi13020337.

(22) Wang, J.; Xiong, Z.; Zhan, X.; Dai, B.; Zheng, J.; Liu, J.; Tang, J. A Silicon Nanowire as a Spectrally Tunable Light-Driven Nanomotor. *Advanced Materials* **2017**, *29* (30), 1701451. https://doi.org/10.1002/adma.201701451.

(23) Wang, Q.; Dong, R.; Wang, C.; Xu, S.; Chen, D.; Liang, Y.; Ren, B.; Gao, W.; Cai, Y. Glucose-Fueled Micromotors with Highly Efficient Visible-Light Photocatalytic Propulsion. *ACS Appl. Mater. Interfaces* **2019**, *11* (6), 6201–6207. https://doi.org/10.1021/acsami.8b17563.

(24) A., M.; J., M.; Ashokkumar, M.; Arunachalam, P. A Review on BiVO 4 Photocatalyst: Activity Enhancement Methods for Solar Photocatalytic Applications. *Applied Catalysis A: General* **2018**, *555*, 47–74. https://doi.org/10.1016/j.apcata.2018.02.010.

(25) Qiao, Z.; Yan, T.; Li, W.; Huang, B. In Situ Anion Exchange Synthesis of In $_2$ S $_3$ /In(OH) $_3$ Heterostructures for Efficient Photocatalytic Degradation of MO under Solar Light. *New J. Chem.* **2017**, *41* (8), 3134–3142. https://doi.org/10.1039/C6NJ04119A.

(26) Kamble, G. S.; Natarajan, T. S.; Patil, S. S.; Thomas, M.; Chougale, R. K.; Sanadi, P. D.; Siddharth, U. S.; Ling, Y.-C. BiVO4 As a Sustainable and Emerging Photocatalyst: Synthesis Methodologies, Engineering Properties, and Its Volatile Organic Compounds Degradation Efficiency. *Nanomaterials* **2023**, *13* (9), 1528. https://doi.org/10.3390/nano13091528.

(27) Tan, H. L.; Amal, R.; Ng, Y. H. Alternative Strategies in Improving the Photocatalytic and Photoelectrochemical Activities of Visible Light-Driven BiVO $_4$: A Review. *J. Mater. Chem. A* **2017**, *5* (32), 16498–16521. https://doi.org/10.1039/C7TA04441K.

(28) Ni, M.; Leung, M. K. H.; Leung, D. Y. C.; Sumathy, K. A Review and Recent Developments in Photocatalytic Water-Splitting Using TiO2 for Hydrogen Production. *Renewable and Sustainable Energy Reviews* **2007**, *11* (3), 401–425. https://doi.org/10.1016/j.rser.2005.01.009.

(29) Li, J.; Wang, F.; Meng, L.; Han, M.; Guo, Y.; Sun, C. Controlled Synthesis of BiVO 4 /SrTiO 3 Composite with Enhanced Sunlight-Driven Photofunctions for Sulfamethoxazole Removal. *Journal of Colloid and Interface Science* **2017**, *485*, 116–122. https://doi.org/10.1016/j.jcis.2016.07.040.

(30) Li, F.; Yang, C.; Li, Q.; Cao, W.; Li, T. The pH-Controlled Morphology Transition of BiVO4 Photocatalysts from Microparticles to Hollow Microspheres. *Materials Letters* **2015**, *145*, 52–55. https://doi.org/10.1016/j.matlet.2015.01.043.

(31) Tücks, A.; Beck, H. P. The Photochromic Effect of Bismuth Vanadate Pigments. Part I: Synthesis, Characterization and Lightfastness of Pigment Coatings. *Journal of Solid-State Chemistry* **2005**, *178* (4), 1145–1156. https://doi.org/10.1016/j.jssc.2004.11.025.

(32) Kudo, A.; Omori, K.; Kato, H. A Novel Aqueous Process for Preparation of Crystal Form-Controlled and Highly Crystalline BiVO $_4$ Powder from Layered Vanadates at Room Temperature and Its Photocatalytic and Photophysical Properties. *J. Am. Chem. Soc.* **1999**, *121* (49), 11459–11467. https://doi.org/10.1021/ja992541y.

(33) Xue, Y.; Wang, X. The Effects of Ag Doping on Crystalline Structure and Photocatalytic Properties of BiVO4. *International Journal of Hydrogen Energy* **2015**, *40* (17), 5878–5888. https://doi.org/10.1016/j.ijhydene.2015.03.028.

(34) Xu, X.; Du, M.; Chen, T.; Xiong, S.; Wu, T.; Zhao, D.; Fan, Z. New Insights into Ag-Doped $BiVO_4$ Microspheres as Visible Light Photocatalysts. *RSC Adv.* **2016**, *6* (101), 98788–98796. https://doi.org/10.1039/C6RA20850A.

(35) Yin, C.; Zhu, S.; Chen, Z.; Zhang, W.; Gu, J.; Zhang, D. One Step Fabrication of C-Doped BiVO4 with Hierarchical Structures for a High-Performance Photocatalyst under Visible Light Irradiation. *J. Mater. Chem. A* **2013**, *1* (29), 8367. https://doi.org/10.1039/c3ta11833a.

(36) Wang, W.; Wang, J.; Wang, Z.; Wei, X.; Liu, L.; Ren, Q.; Gao, W.; Liang, Y.; Shi, H. P–n Junction CuO/BiVO4 Heterogeneous Nanostructures: Synthesis and Highly Efficient Visible-Light Photocatalytic Performance. *Dalton Trans.* **2014**, *43* (18), 6735. https://doi.org/10.1039/c3dt53613k.

(37) Dang, X.; Zhang, X.; Dong, X.; Ruan, W.; Ma, H.; Xue, M. The p–n Heterojunction with Porous $BiVO_4$ Framework and Well-Distributed Co_3O_4 as a Super Visible-Light-Driven Photocatalyst. *RSC Adv.* **2014**, *4* (97), 54655–54661. https://doi.org/10.1039/C4RA11417E.

(38) Gao, X.; Liang, C.; Gao, K.; Li, X.; Liu, J.; Li, Q. Z-Scheme Heterojunction Ag3PO4/BiVO4 with Exposing High-Active Facets and Stretching Spatial Charge Separation Ability for Photocatalytic Organic Pollutants Degradation. *Applied Surface Science* **2020**, *524*, 146506. https://doi.org/10.1016/j.apsusc.2020.146506.

(39) Li, R.; Zhang, F.; Wang, D.; Yang, J.; Li, M.; Zhu, J.; Zhou, X.; Han, H.; Li, C. Spatial Separation of Photogenerated Electrons and Holes among {010} and {110} Crystal Facets of BiVO4. *Nat Commun* **2013**, *4* (1), 1432. https://doi.org/10.1038/ncomms2401.

(40) Heckel, S.; Wittmann, M.; Reid, M.; Villa, K.; Simmchen, J. An Account on $BiVO_4$ as Photocatalytic Active Matter. *Acc. Mater. Res.* **2024**, *5* (4), 400–412. https://doi.org/10.1021/accountsmr.3c00021.

(41) Wu, L.-Y.; Zhang, M.-R.; Feng, Y.-X.; Zhang, W.; Zhang, M.; Lu, T.-B. Two-Dimensional Metal Halide Perovskite Nanosheets for Efficient Photocatalytic CO_2 Reduction. *Solar RRL* **2021**, *5* (8), 2100263. https://doi.org/10.1002/solr.202100263.

(42) Huang, H.; Pradhan, B.; Hofkens, J.; Roeffaers, M. B. J.; Steele, J. A. Solar-Driven Metal Halide Perovskite Photocatalysis: Design, Stability, and Performance. *ACS Energy Lett.* **2020**, *5* (4), 1107–1123. https://doi.org/10.1021/acsenergylett.0c00058.

(43) Slavney, A. H.; Hu, T.; Lindenberg, A. M.; Karunadasa, H. I. A Bismuth-Halide Double Perovskite with Long Carrier Recombination Lifetime for Photovoltaic Applications. *J. Am. Chem. Soc.* **2016**, *138* (7), 2138–2141. https://doi.org/10.1021/jacs.5b13294.

(44) McClure, E. T.; Ball, M. R.; Windl, W.; Woodward, P. M. Cs_2AgBiX_6 (X = Br, Cl): New Visible Light Absorbing, Lead-Free Halide Perovskite Semiconductors. *Chem. Mater.* **2016**, *28* (5), 1348–1354. https://doi.org/10.1021/acs.chemmater.5b04231.

(45) Ding, L.; Bai, F.; Borjigin, B.; Li, Y.; Li, H.; Wang, X. Embedding Cs2AgBiBr6 QDs into Ce-UiO-66-H to in Situ Construct a Novel Bifunctional Material for Capturing and Photocatalytic Reduction of CO2. *Chemical Engineering Journal* **2022**, *446*, 137102. https://doi.org/10.1016/j.cej.2022.137102.

(46) Shivalkar, S.; Gautam, P. K.; Chaudhary, S.; Samanta, S. K.; Sahoo, A. K. Recent Development of Autonomously Driven Micro/Nanobots for Efficient Treatment of Polluted Water. *Journal of Environmental Management* **2021**, *281*, 111750. https://doi.org/10.1016/j.jenvman.2020.111750.

(47) Seiple, I. B.; Zhang, Z.; Jakubec, P.; Langlois-Mercier, A.; Wright, P. M.; Hog, D. T.; Yabu, K.; Allu, S. R.; Fukuzaki, T.; Carlsen, P. N.; Kitamura, Y.; Zhou, X.; Condakes, M. L.; Szczypiński, F. T.; Green, W. D.; Myers, A. G. A Platform for the Discovery of New Macrolide Antibiotics. *Nature* **2016**, *533* (7603), 338–345. https://doi.org/10.1038/nature17967.

(48) Babić, S.; Ćurković, L.; Ljubas, D.; Čizmić, M. TiO2 Assisted Photocatalytic Degradation of Macrolide Antibiotics. *Current Opinion in Green and Sustainable Chemistry* **2017**, *6*, 34–41. https://doi.org/10.1016/j.cogsc.2017.05.004.

(49) Sajid, M. M.; Shad, N. A.; Afzal, A. M.; Javed, Y.; Khan, S. B.; Amin, N.; Shah, A.; Yousaf, I.; Zhai, H. Generation of Strong Oxidizing Radicals from Plate-like Morphology of BiVO4 for the

Fast Degradation of Crystal Violet Dye under Visible Light. *Appl. Phys. A* **2020**, *126* (4), 314. https://doi.org/10.1007/s00339-020-03484-8.

(50) Sajid, M. M.; Khan, S. B.; Shad, N. A.; Amin, N.; Zhang, Z. Visible Light Assisted Photocatalytic Degradation of Crystal Violet Dye and Electrochemical Detection of Ascorbic Acid Using a $BiVO_4$/$FeVO_4$ Heterojunction Composite. *RSC Adv.* **2018**, *8* (42), 23489–23498. https://doi.org/10.1039/C8RA03890B.

(51) Tran, T.-H.; Le, P.-N.-M.; Ngo, T.-H.; Huynh, N.-D.-T.; Oh, W.-C.; Le, M.-V. An Investigation on the Visible Light-Driven Z-Scheme BiVO4/g-C3N4 Heterostructures: Performance, Evaluation, and Mechanism for Dye and Antibiotics Degradation. *Materials Today Communications* **2024**, *40*, 109373. https://doi.org/10.1016/j.mtcomm.2024.109373.

(52) Leite, E. R.; Ribeiro, C. Classical Crystallization Model: Nucleation and Growth. In *Crystallization and Growth of Colloidal Nanocrystals*; SpringerBriefs in Materials; Springer New York: New York, NY, 2012; pp 19–43. https://doi.org/10.1007/978-1-4614-1308-0_3.

(53) Zulfiqar, N.; Nadeem, R.; Musaimi, O. A. Photocatalytic Degradation of Antibiotics via Exploitation of a Magnetic Nanocomposite: A Green Nanotechnology Approach toward Drug-Contaminated Wastewater Reclamation. *ACS Omega* **2024**, acsomega.3c08116. https://doi.org/10.1021/acsomega.3c08116.

(54) Baig, M. M.; Zulfiqar, S.; Yousuf, M. A.; Touqeer, M.; Ullah, S.; Agboola, PhilipsO.; Warsi, M. F.; Shakir, I. Structural and Photocatalytic Properties of New Rare Earth La3+ Substituted MnFe2O4 Ferrite Nanoparticles. *Ceramics International* **2020**, *46* (14), 23208–23217. https://doi.org/10.1016/j.ceramint.2020.06.103.

(55) Sajid, M. M.; Zhai, H.; Alomayri, T.; Khan, S. B.; Javed, Y.; Shad, N. A.; Ishaq, A. R.; Amin, N.; Zhang, Z. Platinum Doped Bismuth Vanadate (Pt/BiVO4) for Enhanced Photocatalytic Pollutant Degradation Using Visible Light Irradiation. *J Mater Sci: Mater Electron* **2022**, *33* (18), 15116–15131. https://doi.org/10.1007/s10854-022-08431-2.

(56) Zhang, L.; Dai, Z.; Zheng, G.; Yao, Z.; Mu, J. Superior Visible Light Photocatalytic Performance of Reticular $BiVO_4$ Synthesized *via* a Modified Sol–Gel Method. *RSC Adv.* **2018**, *8* (19), 10654–10664. https://doi.org/10.1039/C8RA00554K.

(57) Severo, E. D. C.; Abaide, E. R.; Anchieta, C. G.; Foletto, V. S.; Weber, C. T.; Garlet, T. B.; Collazzo, G. C.; Mazutti, M. A.; Gündel, A.; Kuhn, R. C.; Foletto, E. L. Preparation of Zinc Tungstate (ZnWO4) Particles by Solvo-Hydrothermal Technique and Their Application as Support for Inulinase Immobilization. *Mat. Res.* **2016**, *19* (4), 781–785. https://doi.org/10.1590/1980-5373-MR-2015-0100.

(58) Sandhya Kumari, L.; Prabhakar Rao, P.; Narayana Pillai Radhakrishnan, A.; James, V.; Sameera, S.; Koshy, P. Brilliant Yellow Color and Enhanced NIR Reflectance of Monoclinic BiVO4 through Distortion in VO43− Tetrahedra. *Solar Energy Materials and Solar Cells* **2013**, *112*, 134–143. https://doi.org/10.1016/j.solmat.2013.01.022.

(59) Merupo, V.-I.; Velumani, S.; Ordon, K.; Errien, N.; Szade, J.; Kassiba, A.-H. Structural and Optical Characterization of Ball-Milled Copper-Doped Bismuth Vanadium Oxide ($BiVO_4$). *CrystEngComm* **2015**, *17* (17), 3366–3375. https://doi.org/10.1039/C5CE00173K.

(60) Cai, H.; Cheng, L.; Chen, H.; Dou, R.; Chen, J.; Zhao, Y.; Li, F.; Fang, Z. Facile Phase Control and Photocatalytic Performance of BiVO4 Crystals for Methylene Blue Degradation. *IJERPH* **2023**, *20* (4), 3093. https://doi.org/10.3390/ijerph20043093.

(61) Brack, P.; Sagu, J. S.; Peiris, T. A. N.; McInnes, A.; Senili, M.; Wijayantha, K. G. U.; Marken, F.; Selli, E. Aerosol-Assisted CVD of Bismuth Vanadate Thin Films and Their Photoelectrochemical Properties. *Chemical Vapor Deposition* **2015**, *21* (1-2–3), 41–45. https://doi.org/10.1002/cvde.201407142.

(62) Zhao, G.; Wang, M.; Cao, X.; Guo, Y.; Liu, W.; Teng, H. Effects of pH on the Microstructure and Surface Charge of BiVO4 Prepared via Hydrothermal Method: Formation Mechanism and Photocatalytic Performance. *Res Chem Intermed* **2020**, *46* (2), 1487–1506. https://doi.org/10.1007/s11164-019-04046-1.

(63) He, T.; Zhao, Q.; Wu, Q.; Zhang, J.; Ran, F. Surfactant Induced Self-Assembly to Prepare a Vanadium Nitride/N,S Co-Doped Carbon High-Capacitance Anode Material. *Chem. Commun.* **2021**, *57* (79), 10246–10249. https://doi.org/10.1039/D1CC04143F.

(64) Wołowicz, A.; Hubicki, Z. Vanadium(V) Removal from Aqueous Solutions and Real Wastewaters onto Anion Exchangers and Lewatit AF5. *Molecules* **2022**, *27* (17), 5432. https://doi.org/10.3390/molecules27175432.

(65) Sridhar, V.; Park, B.-W.; Guo, S.; Van Aken, P. A.; Sitti, M. Multiwavelength-Steerable Visible-Light-Driven Magnetic CoO–TiO $_2$ Microswimmers. *ACS Appl. Mater. Interfaces* **2020**, *12* (21), 24149–24155. https://doi.org/10.1021/acsami.0c06100.

(66) Wang, Y.; Hernandez, R. M.; Bartlett, D. J.; Bingham, J. M.; Kline, T. R.; Sen, A.; Mallouk, T. E. Bipolar Electrochemical Mechanism for the Propulsion of Catalytic Nanomotors in Hydrogen Peroxide Solutions. *Langmuir* **2006**, *22* (25), 10451–10456. https://doi.org/10.1021/la0615950.

(67) Kosjek, T.; Heath, E. Applications of Mass Spectrometry to Identifying Pharmaceutical Transformation Products in Water Treatment. *TrAC Trends in Analytical Chemistry* **2008**, *27* (10), 807–820. https://doi.org/10.1016/j.trac.2008.08.014.